Engineering ratchet-based particle separation via extended shortcuts to isothermality

Xiu-Hua Zhao [1], Z. C. Tu [1,2] and Yu-Han Ma [1,3,*]

[1] *School of Physics and Astronomy, Beijing Normal University, Beijing 100875, China*

[2] *Key Laboratory of Multiscale Spin Physics (Ministry of Education), Beijing Normal University, Beijing 100875, China*

[3] *Graduate School of China Academy of Engineering Physics, No. 10 Xibeiwang East Road, Haidian District, Beijing 100193, China*

(Received 4 December 2023; revised 17 July 2024; accepted 9 August 2024; published 3 September 2024)

Microscopic particle separation plays a vital role in various scientific and industrial domains. Conventional separation methods relying on external forces or physical barriers inherently exhibit limitations in terms of efficiency, selectivity, and adaptability across diverse particle types. To overcome these limitations, researchers are constantly exploring new separation approaches, among which ratchet-based separation is a noteworthy method. However, in contrast to the extensive numerical studies and experimental investigations on ratchet separation, its theoretical exploration appears weak, particularly lacking in the analysis of energy consumption involved in the separation processes. The latter is of significant importance for achieving energetically efficient separation. In this paper, we propose a nonequilibrium thermodynamic approach, extending the concept of shortcuts to isothermality, to realize controllable separation of overdamped Brownian particles with low energy cost. By utilizing a designed ratchet potential with temporal period τ, we find in the slow-driving regime that the average particle velocity $\bar{v}_s \propto (1 - D/D^*)\tau^{-1}$, indicating that particles with different diffusion coefficients D can be guided to move in distinct directions with a preset D^*. It is revealed that an inevitable portion of the energy cost in separation depends on the driving dynamics of the ratchet, with an achievable lower bound $W_{\mathrm{ex}}^{(\min)} \propto \mathcal{L}^2|\bar{v}_s|$. Here, $\mathcal{L}$ is the thermodynamic length of the driving loop in the parametric space. With a sawtooth potential, we numerically test the theoretical findings and illustrate the optimal separation protocol associated with $W_{\mathrm{ex}}^{(\min)}$. Finally, for practical considerations, we compare our approach with the conventional ratchets in terms of separation velocity and energy consumption. The scalability of the current framework for separating various particles in two-dimensional space is also demonstrated. This paper bridges the gap between thermodynamic process control and particle separation, paving the way for further thermodynamic optimization in ratchet-based particle separation.

DOI: 10.1103/PhysRevE.110.034105

I. INTRODUCTION

The separation of micro- and nanoscale particles holds significant importance across various scientific and industrial domains [1–9]. In the biological field, the separation of bio-samples, such as proteins and DNA fragments, is crucial for disease detection and bioinformatics analysis [10–13]. In environmental science, the separation of contaminants is vital for evaluating environmental protection efforts [14,15]. Additionally, the purification of nanocomponents is essential for the preparation of nanomaterials [3,4]. Numerous physical methods have been investigated for achieving intact particle separation, employing physical fields and/or barriers. Common physical fields include electric, magnetic, gravitational, centrifugal, temperature, and concentration gradients [16–18]. Membranes with specific pore sizes are also widely utilized for particle separation [19–23]. These techniques leverage differences in particle size, shape, charge, electric susceptibility, magnetic susceptibility, and other properties to achieve separation. When evaluating different separation methods, several criteria are considered, including resolution, efficiency, throughput, application range, and economic feasibility [3,18]. While no single method excels in all these aspects, ongoing innovations in physical fields and structural designs of separating equipment continually enhance the effectiveness of particle separation techniques.

Recent years have seen active studies on ratchet-based particle separation [9,24–30], using both numerical and experimental methods, building on the concept of ratchet that dates back to the work of Smoluchowski and Feynman [31–33]. For theoretical convenience, particle motion in ratchet devices is typically modeled as Brownian motion within specific potentials [28,33–43]. These ratchet potentials are usually periodic in time and either periodic or tilted periodic in space. In practical applications, ratchet potentials can be created using tunable external fields or carefully designed geometric structures that particles encounter in fluidic environments [25,29,35,44–51]. Directed motion arises due to the breaking of spatial and/or temporal symmetry of the ratchet potentials as well as the presence of thermal fluctuations [33,50,52]. The magnitudes of directed particle fluxes depend on the particles' diffusion coefficients and their responses to the applied ratchet potential, enabling particle separation [35,44–48]. The phenomenon of velocity inversion, which occurs as the parameters of the potential or environment change, further enhances the application of ratchets in particle separation [30,37,50]. Since different particles experience velocity

*Contact author: yhma@bnu.edu.cn

inversion at different parameter sets, separation in opposite directions is possible. Despite extensive theoretical studies on ratchets, few specifically focus on particle separation, and even fewer address the energy consumption associated with this process. From a thermodynamic standpoint, the latter is crucial for achieving energetically efficient separation [5,53–55]. Precise theoretical predictions of ratchet-based particle separation will greatly facilitate the comprehensive optimization of ratchet potentials and the enhancement of separation performance.

The main difficulty hindering theoretical studies on ratchet-based particle separation lies in capturing the nonequilibrium evolution in time-dependent potentials, a common challenge in nonequilibrium systems. Recently, the rapidly developed field of thermodynamic process control, known as swift state-to-state transformations, has inspiringly addressed this difficulty through the concept of inverse engineering [56,57]. Instead of solving the evolution with a given dynamic equation, inverse engineering aims to design the equation to achieve the desired evolution. Various specific formalisms based on this engineering strategy have been demonstrated successfully in different systems, including quantum, Hamiltonian, and stochastic systems [58–64]. In these regimes, the driving terms in the dominant equations are typically divided into two parts: a reference term, explicitly related to the system's evolution function, and an auxiliary term designed to escort the evolution. Given the widespread success in controlling nonequilibrium evolution with well-designed interactions or external potentials, it is intriguing to explore the impact of introducing an auxiliary potential into the ratchet-based particle separation scheme.

In this paper, we adopt the auxiliary potential in the form of shortcuts to isothermality (ScI) [63,65], a well-developed thermodynamic control strategy for Brownian particles. While the original ScI theory is applicable to single-type particle schemes [63], simultaneous consideration of multitype particles is necessary for the separation tasks. We investigate the motion of overdamped Brownian particles with varying diffusion coefficients, driven by a potential that combines a conventional ratchet potential with an auxiliary potential featuring a tunable reference diffusion coefficient. Our results demonstrate that particle separation is achieved in a tractable regime, namely, the slow-driving regime, where the average steady-state particle flux depends linearly on the diffusion coefficient. Particles with diffusion coefficients larger or smaller than the reference diffusion coefficient move in opposite directions, resulting in spatial separation. These opposite movements can be attributed to effective forces experienced by the particles dependent on their diffusion coefficients, as illustrated in Fig. 1(a). Simulation results depicted in Fig. 1(b) clearly demonstrate efficient separation of various particle types in two-dimensional space. The energetic cost associated with the separation process is also determined. By utilizing the tool of thermodynamic geometry [64,66–68], we further derive the optimal driving protocol to minimize energy dissipation while maintaining particle flux. These analytical findings, facilitated by the capabilities of ScI-assisted ratchet potentials, enhance our understanding and practical optimization of ratchet-based separation, reducing the need for extensive numerical explorations or experimental investigations.

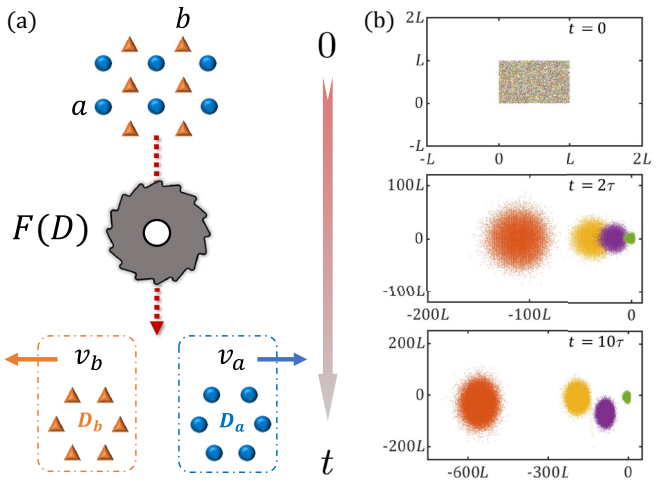

FIG. 1. (a) Schematic diagram of ratchet-based particle separation using the shortcuts to isothermality. With the designed potential, particles with different diffusion coefficients experience distinct driving forces (see Appendix B 2), enabling directed movement in different directions. (b) Two-dimensional separation of four types of particles (see Sec. IV B for details). L and τ represent the spatial and temporal periods of the ratchet potential, respectively.

The rest of this paper is organized as follows. In Sec. II, we present the general theoretical framework of particle separation using ScI-assisted ratchets. The particle separation velocity and the corresponding energetic cost are analytically obtained. Then, in Sec. III, with a specific form of the ratchet potential (sawtooth potential), the general framework is illustrated and verified by numerical simulations. Furthermore, we discusses several practical considerations about the proposed ScI-assisted ratchets in Sec. IV, including comparisons of separation velocities and energy cost between the current framework and conventional ratchets, as well as extensions to two-dimensional separations. The summary and discussion of the current work is given in Sec. V.

II. GENERAL FRAMEWORK

In this section, we incorporate the theoretical structure of ScI into ratchet-based particle separation and analyze two essential quantities in the separation process: particle flux and energetic cost.

Consider one-dimensional overdamped Brownian particles with diffusion coefficient D, which are coupled to a bath at temperature T and experience time-dependent potential $U(x,t)$. The evolution of the particles is governed by the overdamped Fokker-Planck equation [69],

$$\partial_t \rho(x,t) = -\partial_x \hat{J}_t \rho(x,t), \tag{1}$$

where $\rho(x,t)$ is the probability density of the particle at time t and position x,

$$\hat{J}_t \equiv -D[\beta \partial_x U(x,t) + \partial_x] \tag{2}$$

is the current operator, and $\beta \equiv 1/(k_B T)$ is the inverse temperature, with k_B being the Boltzmann constant. In the original ScI framework [63,64], the total potential $U(x,t)$ consists of an original potential $U_o(x,\vec{\lambda})$, where $\vec{\lambda} = \vec{\lambda}(t)$ is a

time-dependent parametric vector with N components, and an auxiliary potential $U_a(x,\vec{\lambda},\dot{\vec{\lambda}})$, where $\dot{\mathcal{O}}$ represents the time derivative of an arbitrary physical quantity $\mathcal{O}$. The auxiliary potential depends on the particle's diffusion coefficient, ensuring that the system evolves along the instantaneous equilibrium distribution of $U_o(x,\vec{\lambda})$, regardless of how $\vec{\lambda}$ varies. To extend ScI into a particle separation scheme that involves multitype particles, we replace the diffusion coefficient in $U_a(x,\vec{\lambda},\dot{\vec{\lambda}})$ tailored for specific particles with a reference diffusion coefficient D^*. The auxiliary potential, now represented as $U_a^*(x,\vec{\lambda},\dot{\vec{\lambda}})$, is in the form of

$$\partial_x U_a^*(x,\vec{\lambda},\dot{\vec{\lambda}}) = \frac{1}{\beta D^*}\frac{\dot{\vec{\lambda}}\cdot[\vec{f}_o(x,\vec{\lambda})+\vec{j}(\vec{\lambda})]}{\rho_o(x,\vec{\lambda})}. \tag{3}$$

Here, $\rho_o(x,\vec{\lambda}) \equiv e^{-\beta U_o(x,\vec{\lambda})}/\int_0^L e^{-\beta U_o(x,\vec{\lambda})}dx$ is the normalized equilibrium probability density over one period $0 \leqslant x \leqslant L$ of the conventional periodic ratchet potential $U_o(x,\vec{\lambda})$ with spatial period L; $\vec{f}_o(x,\vec{\lambda}) \equiv \int_0^x \vec{\nabla}_\lambda \rho_o(x',\vec{\lambda})dx'$, where $\vec{\nabla}_\lambda \equiv (\partial_{\lambda_1},\partial_{\lambda_2},\ldots,\partial_{\lambda_N})$; and $\vec{j}(\vec{\lambda})$ is an arbitrary x-independent N-dimensional vector function. The total potential experienced by the particles is $U(x,t) = U^*(x,t) = U_o(x,\vec{\lambda}) + U_a^*(x,\vec{\lambda},\dot{\vec{\lambda}})$.

A. Particle evolution in designed ratchet potential

The particle's evolution is solved by substituting the expression of the total potential into Eq. (1). Given that $U_o(x,\vec{\lambda})$ and $\partial_x U_a^*(x,\vec{\lambda},\dot{\vec{\lambda}})$ are both periodic, and so is the current operator, it suffices to solve Eq. (1) within one period $x \in [0,L]$ [33]. Specifically, we define the reduced probability density and the reduced probability current, respectively, as $\rho_s(x,t) \equiv \sum_n \rho(x+nL,t)$ and $J_s(x,t) \equiv \sum_n J(x+nL,t)$, where $n \in \mathbb{Z}$ and the probability current reads

$$J(x,t) = \hat{J}_t \rho(x,t). \tag{4}$$

Providing that $\rho(x,t)$ is a normalized solution of Eq. (1), $\rho_s(x,t)$ is also a solution which satisfies the periodic condition $\rho_s(x,t) = \rho_s(x+L,t)$ as well as the conservation condition $\int_0^L \rho_s(x,t)dx = 1$. Moreover, the relation between $\rho_s(x,t)$ and $J_s(x,t)$ is the same as Eq. (4).

To carry out further analytical discussion, we assume that the parametric vector $\vec{\lambda}$ changes slowly over time, so $\rho_s(x,t)$ can be expanded up to the linear term of $\dot{\vec{\lambda}}$ [70,71] as follows:

$$\rho_s(x,t) \approx \rho_o(x,\vec{\lambda}) + \dot{\vec{\lambda}}\cdot\vec{\psi}(x,t), \tag{5}$$

where $\vec{\psi}(x,t)$ is an N-dimensional vector function to be solved. The equilibrium state is recovered when $\dot{\vec{\lambda}} = 0$. Substituting Eq. (5) into Eq. (1) and neglecting the terms containing quadratic time derivative, we obtain

$$\frac{\partial\vec{\psi}(x,t)}{\partial x} + \beta\frac{\partial U_o}{\partial x}\vec{\psi}(x,t) = \left(\frac{1}{D}-\frac{1}{D^*}\right)[\vec{f}_o(x,\vec{\lambda})+\vec{C}(t)], \tag{6}$$

with $\vec{C}(t)$ the constant of integration. Solving Eq. (6) with boundary conditions $\vec{\psi}(0,t) = \vec{\psi}(L,t)$ and $\int_0^L \vec{\psi}(x,t)dx = 0$, we find $\vec{C}(t) = -\langle\vec{f}_o(x,\vec{\lambda})\rangle_+$, where $\langle\cdots\rangle_\pm \equiv \int_0^L e^{\pm\beta U_o(x,\vec{\lambda})}\cdots dx/Z_\pm(\vec{\lambda})$ and $Z_\pm(\vec{\lambda}) \equiv \int_0^L e^{\pm\beta U_o(x,\vec{\lambda})}dx$. The derivation details and the exact form of $\vec{\psi}(x,t)$ is given in Appendix A. It follows from Eqs. (4) and (6) that

$$J_s(x,t) = -\dot{\vec{\lambda}}\cdot\vec{f}(x,\vec{\lambda}) + \left(1-\frac{D}{D^*}\right)\dot{\vec{\lambda}}\cdot\langle\vec{f}(x,\vec{\lambda})\rangle_+, \tag{7}$$

where $\vec{f}(x,\vec{\lambda}) \equiv \vec{f}_o(x,\vec{\lambda}) + \vec{j}(\vec{\lambda})$. Then the ensemble-averaged velocity of the particle flux is given by $v_s(t) \equiv \int_0^L J_s(x,t)dx$ [69].

B. Separating particles with different diffusion coefficients

We then investigate the particle flux in the steady state. To induce steady-state evolution, we consider that the Brownian particles are periodically driven, namely, $\vec{\lambda}(t) = \vec{\lambda}(t+\tau)$ and $\dot{\vec{\lambda}}(t) = \dot{\vec{\lambda}}(t+\tau)$ with the temporal period τ. After enough periods, $\rho_s(x,t)$ will enter steady periodic evolution (5) independent of the initial condition. It follows from Eq. (7) that the average reduced probability current over a temporal period $\bar{J}_s \equiv \tau^{-1}\int_{t_0}^{t_0+\tau} J_s(x,t)dt$ is specifically obtained as

$$\bar{J}_s = \frac{1}{\tau}\left(1-\frac{D}{D^*}\right)\Phi_{\rm rev} - \frac{1}{\tau}\frac{D}{D^*}\oint_I d\vec{\lambda}\cdot\vec{j}(\vec{\lambda}), \tag{8}$$

where

$$\Phi_{\rm rev} \equiv \oint_I d\vec{\lambda}\cdot\frac{\int_0^L e^{\beta U_o(x,\vec{\lambda})}\vec{\nabla}_\lambda\int_0^x \rho_o(x',\vec{\lambda})dx'dx}{\int_0^L e^{\beta U_o(x,\vec{\lambda})}dx} \tag{9}$$

is the nondimensional integrated flow of reversible ratchets [40,72] and I is a closed trajectory of $\vec{\lambda}$ in the parametric space. The derivation of Eq. (8) can be found in Appendix B 1. Noticing that $\bar{J}_s$ is independent of x, which is characteristic of periodic evolution, the time-ensemble-averaged velocity becomes $\bar{v}_s \equiv \tau^{-1}\int_{t_0}^{t_0+\tau} v_s(t)dt = \bar{J}_s L$.

As one of the main results of this paper, Eq. (8), applicable to arbitrary $U_o(x,\vec{\lambda})$, indicates that Brownian particles with different D can move at different velocities on average, thereby enabling their spatial separation. Physically, the directed motion of particles is governed by an effective force defined as $F_{\rm eff} \equiv \tau^{-1}\int_{t_0}^{t_0+\tau}\int F(x,t)\rho(x,t)dx\,dt$, where $F(x,t)$ is the instantaneous force experienced by the particles. This effective force is in the same direction as the average particle flux, with detailed derivations provided in Appendix B 2. We stress here that (i) to generate nonzero $\Phi_{\rm rev}$, a spatially asymmetric $U_o(x,\vec{\lambda})$ is necessary (Proof is given in Appendix B 3) and (ii) since $\Phi_{\rm rev}$ and $\bar{J}_s$ are geometric quantities in the N-dimensional parametric space that only depend on the geometry of I, $N \geqslant 2$ is required to result in nonzero $\Phi_{\rm rev}$ and $\bar{J}_s$. Particularly, when $\vec{j}(\vec{\lambda}) = 0$, the particles with $D > D^*$ and those with $D < D^*$ will move in opposite directions, which is consistent with a recent numerical study [30]. In the cases with $\vec{j}(\vec{\lambda}) \neq 0$, particles may be separated with velocities different in magnitude but in the same direction, as illustrated in Sec. III B.

Moreover, it is worth mentioning that some previous theoretical results obtained in the solvable slow-driving regime for conventional ratchets [38,40,73], which do not depend on

the diffusion coefficient, indicate that even though slow-driven conventional ratchets allow for directed particle transport, they may fail to separate different particles with various D. The particle separation demonstrated here is made possible by the assistance of ScI-type auxiliary potential. In real-world circumstances, different types of particles possess different D due to variations in their shape, size, surface structure, and other characteristics [74,75]. Therefore, by choosing an appropriate D^* to design $U_a^*(x,\vec{\lambda},\dot{\vec{\lambda}})$ according to Eq. (3), the desired particle separation can be achieved.

C. Energetic cost for particle separation

Besides the separation velocity discussed above, the energy consumption in driving the particles is another typical aspect of thermodynamic analysis requiring significant attention, a quantity that can be analyzed with stochastic thermodynamics [76,77]. When the particles of interest have entered the steady periodic state, their energetics may be captured through the above-solved reduced probability density and reduced probability current. According to the first law of thermodynamics, the ensemble-averaged work needed in driving the particle is $W=\Delta E-Q$, where Q is the ensemble-averaged heat absorbed by the particle and ΔE is the variation of internal energy $E(t)\equiv\int U^*(x,t)\rho(x,t)dx$. The total potential $U^*(x,t)$ obtained by adding the integral of Eq. (3) on $U_o(x,\vec{\lambda})$ is a tilted ratchet potential

$$U^*(x,t)=V^*(x,t)+\frac{\varepsilon^*(t)}{L}x, \tag{10}$$

where

$$\varepsilon^*(t)=\frac{Z_-(\vec{\lambda})Z_+(\vec{\lambda})\dot{\vec{\lambda}}\cdot\langle\vec{f}(x,\vec{\lambda})\rangle_+}{\beta D^*} \tag{11}$$

is the variation of $U_a^*(x,t)$ from x_0 to x_0+L, and

$$V^*(x,t)\equiv U_o(x,\vec{\lambda})+\int_0^x\partial_{x'}U_a^*(x',t)dx'-\frac{\varepsilon^*(t)x}{L} \tag{12}$$

is a spatially periodic function with period L. Here, we have set $U_a^*(0,t)=0$. Then the internal energy of the particle turns out to be

$$E(t)=\int_0^L V^*(x,t)\rho_s(x,t)dx+\frac{\varepsilon^*(t)}{L}\langle x\rangle_t, \tag{13}$$

with $\langle x\rangle_t\equiv\int x\rho(x,t)dx$ being the ensemble-averaged position of the particle. A detailed derivation of the above expression is presented in Appendix C 1. For periodic driving with $\vec{\lambda}(t_0)=\vec{\lambda}(t_0+\tau)$ and $\dot{\vec{\lambda}}(t_0)=\dot{\vec{\lambda}}(t_0+\tau)$, the variation of the first term in Eq. (13) vanishes in a temporal period. Noticing that $\varepsilon^*(t_0)=\varepsilon^*(t_0+\tau)$ and $\Delta\langle x\rangle_t=\bar{v}_s\tau$, the variation of internal energy in a period is

$$\Delta E=\varepsilon^*(t_0)\bar{J}_s\tau=\left(1-\frac{D}{D^*}\right)\varepsilon^*(t_0)\Phi_{\rm rev}. \tag{14}$$

Hereafter, unless otherwise stated, we take $\vec{j}(\vec{\lambda})=0$ for simplicity and the general cases with $\vec{j}(\vec{\lambda})\neq 0$ can be found in the detailed derivations in the Appendices. While the above result may depend on the initial conditions of the driving protocol, there is no need to be concerned about the randomness of the initial moments affecting the energy analyses in practical implementations, since this dependence diminishes as the particle transport duration increases. Considering $t_0\in(0,\tau)$ is a random moment taken as the initial time, the variation of the internal energy from t_0 to $N\tau$ is

$$E(N\tau)-E(t_0)=N\varepsilon^*(0)\bar{J}_s\tau\left(1+\frac{E(0)-E(t_0)}{N\varepsilon^*(0)\bar{J}_s\tau}\right), \tag{15}$$

where we have used $E(N\tau)-E(0)=N[E(\tau)-E(0)]$ and $E(\tau)-E(0)=\varepsilon^*(0)\bar{J}_s\tau$. When $N\gg 1$, the average energy consumption per single period becomes $[E(N\tau)-E(t_0)]/N\approx\varepsilon^*(0)\bar{J}_s\tau$, which is independent of t_0.

Furthermore, the heat current reads [76,77]

$$\dot{Q}(t)\equiv\int U^*(x,t)\partial_t\rho(x,t)dx, \tag{16}$$

according to which the heat absorption in a temporal period is obtained as (see Appendix C 2)

$$Q=-\int_{t_0}^{t_0+\tau}dt\dot{\lambda}_\alpha\dot{\lambda}_\beta G_{\alpha\beta}(\vec{\lambda}). \tag{17}$$

The Einstein notation has been adopted hereafter, and

$$G_{\alpha\beta}(\vec{\lambda})\equiv\frac{1}{\beta D^*}Z_-(\vec{\lambda})Z_+(\vec{\lambda})\Big[\langle f_\alpha(x,\vec{\lambda})f_\beta(x,\vec{\lambda})\rangle_+ - \left(1-\frac{D}{D^*}\right)\langle f_\alpha(x,\vec{\lambda})\rangle_+\langle f_\beta(x,\vec{\lambda})\rangle_+\Big] \tag{18}$$

is a positive semidefinite matrix with $\alpha,\beta=1,2,\ldots,N$ (see Appendix C 3 for proof). Hence, the particles release heat to the environment on average.

For a given closed driving trajectory in the parametric space, Cauchy-Schwarz inequality implies that the heat release in Eq. (17) is bounded from below as $-Q\geqslant\mathcal{L}^2/\tau$, where $\mathcal{L}\equiv\int_0^\tau dt\sqrt{\dot{\lambda}_\alpha\dot{\lambda}_\beta G_{\alpha\beta}(\vec{\lambda})}$ is the so-called thermodynamic length [64,66–68,71] of the driving loop. Therefore, we have the work cost satisfying $W\geqslant\Delta E+\mathcal{L}^2/\tau$, which, together with Eq. (8), yields the second main result of this paper (see Appendix C 4 for derivation):

$$W\geqslant\Delta E+\frac{D^*\mathcal{L}^2\bar{J}_s}{(D^*-D)\Phi_{\rm rev}}. \tag{19}$$

Note that the extra energetic cost as $W_{\rm ex}\equiv W-\Delta E$, which is exactly equal to the heat dissipated to the bath, is proportional to the irreversible entropy production in the slow-driving regime [78]. Moreover, when the equal sign in the above inequality is saturated, the minimal extra energetic cost for particle separation is directly proportional to the particle flow, namely, faster particle separation (shorter τ) requires more work consumption. For a given τ (corresponds to a certain $\bar{v}_s$), the optimal driving protocol associated with the minimal $W_{\rm ex}$ is determined by

$$\tau\sqrt{\dot{\lambda}_\alpha\dot{\lambda}_\beta G_{\alpha\beta}(\vec{\lambda})}-\mathcal{L}=0, \tag{20}$$

namely, the integrand of $\mathcal{L}$ is a time-independent constant [67,68].

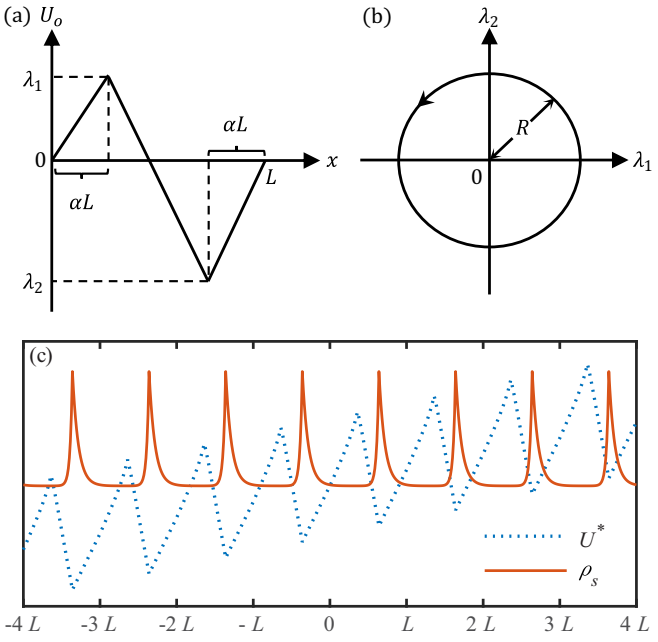

FIG. 2. (a) One period of the original periodic potential $U_o(x, \vec{\lambda})$. (b) The trajectory of the driving protocol $\vec{\lambda}(t)$ is an anticlockwise circle with radius R. (c) The tilted total potential $U^*(x, t)$ and the periodic steady reduced probability density $\rho_s(x, t)$ at a certain time.

III. ILLUSTRATIONS WITH A SAWTOOTH POTENTIAL

To illustrate our general theoretical framework, we specify $U_o = U_o(x, \vec{\lambda})$ as the sawtooth potential in this section. As one of the most commonly used ratchet potentials, the sawtooth potential shown in Fig. 2(a) reads

$$U_o(x,\vec{\lambda}) = \begin{cases} \frac{\lambda_1}{\alpha}\frac{x}{L}, & 0 \leqslant \frac{x}{L} \leqslant \alpha \\ \lambda_1 + \frac{\lambda_2-\lambda_1}{1-2\alpha}\left(\frac{x}{L}-\alpha\right), & \alpha < \frac{x}{L} \leqslant 1-\alpha \\ \lambda_2 - \frac{\lambda_2}{\alpha}\left(\frac{x}{L}-1+\alpha\right), & 1-\alpha < \frac{x}{L} \leqslant 1, \end{cases} \tag{21}$$

where λ_1 and λ_2 serve as time-dependent parameters, i.e., $\vec{\lambda} = (\lambda_1, \lambda_2)$, and $\alpha \in (0, 0.5)$ is a tunable parameter. The expressions for $Z_\pm(\vec{\lambda})$, $\rho_o(x, \vec{\lambda})$, and $\vec{f}_o(x, \vec{\lambda})$ are coherently derived from $U_o(x, \vec{\lambda})$ to obtain $U_a^*(x, \vec{\lambda}, \dot{\vec{\lambda}})$, which is shown in Appendix D 1.

According to Eqs. (8) and (9), $U_o(x, \vec{\lambda})$ is related to the average particle probability current through Φ_{rev}. Therefore, optimizing both the shape of the potential and the geometry of the driving loop in the parametric space can induce a large particle flux. In the two-dimensional parametric space (λ_1, λ_2), using Green's theorem, Eq. (9) turns out to be

$$\Phi_{\text{rev}} = \iint_\Sigma \left(\frac{\partial C_1}{\partial \lambda_2} - \frac{\partial C_2}{\partial \lambda_1}\right) d\lambda_1 d\lambda_2, \tag{22}$$

where $(C_1, C_2) = \vec{C}(\vec{\lambda}) = -\langle \vec{f}_o(x, \vec{\lambda})\rangle_+$, and Σ is the region enclosed by the driving loop I. To find favorable α and the driving loop, we calculate $(\partial_{\lambda_2} C_1 - \partial_{\lambda_1} C_2)$ on the parametric space and Φ_{rev} at different α. The corresponding figures are provided in Appendix D 2. It is found that $(\partial_{\lambda_2} C_1 - \partial_{\lambda_1} C_2)$ is always positive and exhibits large values within a closed region containing the origin in the parametric space. Hence, it is reasonable to choose the circle with a radius R and a center at the origin as the driving loop I, as shown in Fig. 2(b). In addition, the nondimensional quantity $\beta^{-2}(\partial_{\lambda_2} C_1 - \partial_{\lambda_1} C_2)$ is rather small when $\beta\lambda_{1,2} > 7$, so we set $\beta R = 7$. Then the maximum value of Φ_{rev} as a function of α appears around $\alpha = 0.36$, which is adopted as the value of α in the following simulations. In Fig. 2(c), we present a snapshot of the total potential $U^*(x, t)$ and the steady reduced probability density $\rho_s(x, t)$. Both $\rho_s(x, t)$ and the gradient of $U^*(x, t)$ exhibit periodic behavior in infinite space.

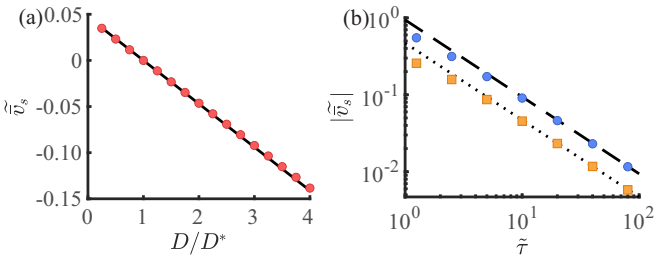

FIG. 3. The time-ensemble-averaged velocity of particles. (a) The time-ensemble-averaged velocity $\widetilde{v}_s$ as a function of D/D^* with $\tilde{\tau} = 20$. (b) $\widetilde{v}_s$ as a function of $\tilde{\tau}$ for $D/D^* = 2$ (circles and dashed line) and $D/D^* = 1/2$ (squares and dotted line). The marks and lines are simulation results and analytical predictions, respectively. In the simulations, characteristic quantities are set as $L = 1$, $\beta = 1$, and $D^* = 1$.

The dynamic equation governing the movement of the overdamped Brownian particles reads [79]

$$\dot{x} = -\beta D \partial_x U^*(x, t) + \sqrt{2D}\xi(t), \tag{23}$$

where the normalized Gaussian white noise $\xi(t)$ satisfies $\langle \xi(t)\rangle = 0$ and $\langle \xi(t)\xi(t')\rangle = \delta(t - t')$. We simulate the movement of the particles by solving this equation with the Euler algorithm [80]:

$$\Delta\tilde{x} = -\tilde{D}\frac{\partial \tilde{U}^*(\tilde{x}, \tilde{t})}{\partial \tilde{x}}\Delta\tilde{t} + \sqrt{2\tilde{D}\Delta\tilde{t}}\omega(\tilde{t}). \tag{24}$$

Here, $\omega(\tilde{t})$ is a standard Gaussian random variable and $\tilde{\mathcal{O}}$ denotes the dimensionless $\mathcal{O}$, nondimensionalized by three characteristic quantities L, β^{-1}, and D^*. For example, $\tilde{t} = D^* L^{-2} t$, $\tilde{x} = L^{-1}x$, $\tilde{D} = D^{*-1}D$, $\tilde{U}^* = \beta U^*$, and $\widetilde{v}_s \equiv D^{*-1}L v_s$. In the following simulations, we set the number of particles to $N = 10^5$ and the time step to $\Delta\tilde{t} = 10^{-4}$.

A. Separation velocity and energy cost

After confirming that the steady-state distribution of the particles is indeed consistent with Eq. (5) in the slow driving regime (shown in Appendix D 3), we first validate the effectiveness of Eq. (8). The time-ensemble-averaged velocities $\bar{v}_s = \bar{J}_s L$ of particles for different diffusion coefficients are plotted in Fig. 3(a). The theoretical prediction (solid line) is in good alignment with the simulation data (circles). In Fig. 3(b), we illustrate $\widetilde{v}_s$ as a function of $\tilde{\tau}$ for $D/D^* = 2$ (circles) and $D/D^* = 1/2$ (squares). As expected, the theoretical lines coincide well with the simulated marks in the slow-driving regime ($\tilde{\tau} \gg 1$).

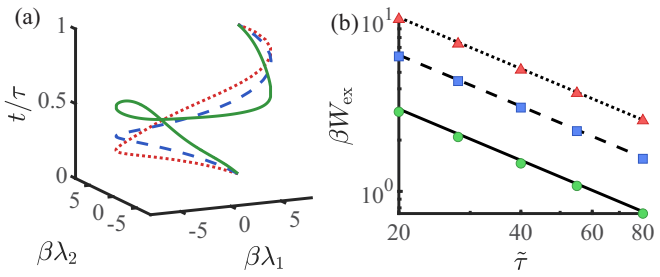

FIG. 4. Dependence of energy consumption in particle separation on driving protocols and duration. (a) Three different driving protocols, i.e., path I (dotted line), path II (dashed line), and path III (solid line). (b) The extra energetic cost W_{ex} as a function of $\tilde{\tau}$ with $D/D^* = 2$. The three data series from top to bottom, respectively, correspond to paths I–III, and the lines are analytical results. The other parameters in the simulations are the same as those used in Fig. 3.

Furthermore, by definition [76], the energetics of the particle can be consistently obtained in simulations. The absorbed heat and the input work of a particle from t to $t + \Delta t$ with position changing from x to $x + \Delta x$ are, respectively,

$$\Delta q \equiv U^*(x + \Delta x, t + \Delta t) - U^*(x, t + \Delta t), \tag{25}$$

$$\Delta w \equiv U^*(x, t + \Delta t) - U^*(x, t), \tag{26}$$

representing the energy changes due to the variation of the particle state and the potential parameters. Clearly, these definitions ensure the energy conservation law $\Delta U^* = \Delta q + \Delta w$ for each particle. Moreover, the ensemble average of $\Delta q/\Delta t$ aligns with the continuous form of heat current (16) as $\Delta t \to 0$ (see Appendix D 4 for proofs). We now test Eq. (19) with three different protocols $f(s)$ associated with the driving loop illustrated in Fig. 2(b),

$$\lambda_1 = R\cos[2\pi f(s) + \theta_0],\ \lambda_2 = R\sin[2\pi f(s) + \theta_0], \tag{27}$$

where $s \equiv t/\tau$ and $\theta_0 = \pi/6$. The time-dependent paths are demonstrated in Fig. 4(a). Path I (dotted line): $f_1(s) = \sum_{i=1}^{i=3} a_i s^i$, with $a_1 = a_3 = 2, a_2 = -3$; path II (dashed line): $f_2(s) = s$; and path III (solid line): the optimal protocol obtained numerically from Eq. (20) (see Appendix D 5 for details). All three protocols satisfy the periodic conditions for $\lambda_\mu(s)$ and $d\lambda_\mu/\mathrm{ds}$, where $\mu = 1, 2$. The corresponding extra work W_{ex} are illustrated in Fig. 4(b) with same line styles, where the dotted and dashed lines [plotted with Eq. (17)] and the solid line [the lower bound of Eq. (19)] agree well with the numerical results (marks). Clearly, the optimal protocol indeed lead to lower W_{ex} (circles) than those associated with path I (triangles) and path II (squares).

We would like to make three remarks here. First, although generated under path II, the results in Figs. 3(a) and 3(b) are independent of the specific choice of driving protocol $f(s)$ since the time-ensemble-averaged velocity is a geometric quantity (dynamic independent) in the parametric space. Second, in the slow-driving regime, the $1/\tau$-scaling exhibited by the particle flux [Fig. 3(b)] and energetic cost [Fig. 4(b)] is a typical manifestation of finite-time irreversibility [63,64,71,78,81–83]. Third, the presented optimal path [solid line in Fig. 4(a)] is associated with the minimum W_{ex} along a given trajectory in the parametric space. There may be

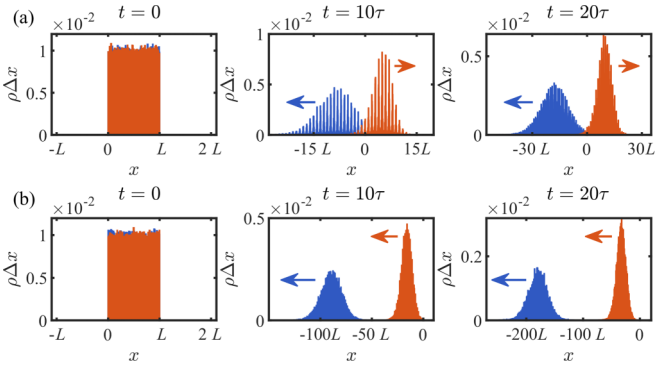

FIG. 5. Probability distributions of particles with $D/D^* = 2$ (blue lines, on the left when $t > 0$) and $D/D^* = 1/2$ (orange lines, on the right when $t > 0$) driven by potentials with different $\vec{j}(\vec{\lambda})$. The width of the histogram bars is $\Delta x = 10^{-2}L$. The arrows indicate the moving directions of the two particles, with the length of the arrows representing the relative magnitudes of their velocities in each panel. (a) $\vec{j}(\vec{\lambda}) = 0$; (b) $j_1(\vec{\lambda}) = -\beta^2\lambda_2/75$, $j_2(\vec{\lambda}) = \beta^2\lambda_1/75$. In this plot, we use $\tau = 10D^{*-1}L^2$, $\beta = D^* = L = 1$, and the driving protocol follows path II.

different trajectories leading to the same particle flux but with different energy cost. Determining the optimal trajectory and the corresponding optimal driving protocol is an open question for achieving globally optimal control in both dynamic and geometric senses.

B. Same-direction separation with nonzero $\vec{j}(\vec{\lambda})$

As a final illustration in this section, we demonstrate the role of $\vec{j}(\vec{\lambda})$ in inducing rapid same-direction separation. According to Eq. (8), $\vec{j}(\vec{\lambda})$ can be utilized to induce a D-dependent probability current and hence particle flux. If $\vec{j}(\vec{\lambda}) = 0$, the particles with $D > D^*$ and $D < D^*$ averagely move in opposite directions; if $\vec{j}(\vec{\lambda}) \neq 0$, it is more possible that the particles with different D move in the same direction, with separation occurring due to differences in their velocity magnitudes. As an example, Figs. 5(a) and 5(b) respectively show the probability distributions of two different particles driven by the potentials with $\vec{j}(\vec{\lambda}) = 0$ and $\vec{j}(\vec{\lambda}) = (-\beta^2\lambda_2/75, \beta^2\lambda_1/75)$. The former scenario facilitates the handling of separated particles due to their opposite destinations, while the latter scenario results in significantly faster separation.

IV. PRACTICAL APPLICATIONS

In this section, we present further discussions concerning the practicality of our proposed separation scheme based on ScI-assisted ratchets. First, according to Eq. (8), the velocity difference $\Delta\bar{v}_s = \Delta\bar{J}_s L$ of particles with diffusion coefficient difference ΔD, is specifically

$$\Delta\bar{v}_s = \frac{-\Delta D L}{D^*\tau}\left[\Phi_{\mathrm{rev}} + \oint_I d\vec{\lambda}\cdot\vec{j}(\vec{\lambda})\right]. \tag{28}$$

For the practical case with $D^* \sim 10^{-5}\,\mathrm{cm}^2/\mathrm{s}$, $L \sim 0.1\,\mu\mathrm{m}$, $f = \tau^{-1} \sim 100\,\mathrm{kHz}$ [30], $\Delta D/D^* \sim 1\%$ can result

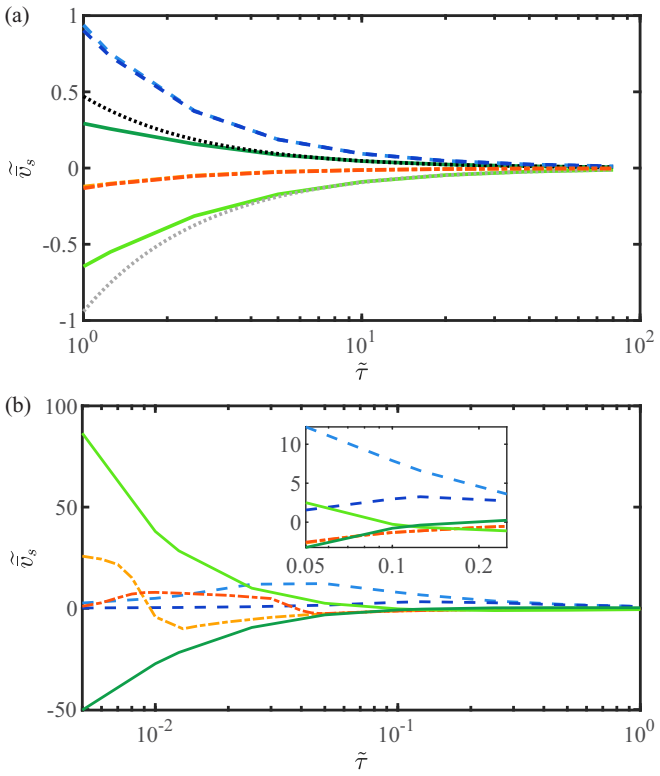

FIG. 6. The average velocities of two different particles driven by different ratchets in (a) slow-driving regime and (b) fast-driving regime. The green solid lines, blue dashed lines, and orange dash-dotted lines represent the velocities induced by $U^*(x,t)$, $U_o(x,t)$, and $U_s(x,t)$, respectively. The dotted lines in (a) are the analytical predictions for $U^*(x,t)$. The lines with dark colors correspond to the particles with $D/D^* = 1/2$, while those with light colors correspond to $D/D^* = 2$. In this plot, $\tilde{\tau} \equiv D^* L^{-2}\tau$, $\tilde{\bar{v}}_s \equiv D^{*-1}L\bar{v}_s$, and the particle number $N = 10^5$. The driving protocols of $U^*(x,t)$ and $U_o(x,t)$ follow path II and $\vec{j}(\vec{\lambda}) = 0$.

in a velocity difference of at least $|\Delta\bar{v}_s| \sim 0.1$ mm/s, which is achieved when $\Phi_{\text{rev}} \sim 1$ [see Fig. 9(b)] and $\vec{j}(\vec{\lambda}) = 0$.

A. Comparison with conventional ratchets

In addition to simplifying theoretical analysis, we find that the ScI-assisted ratchet may outperform conventional ratchets in terms of both separation velocity and energetic cost. We simulate the movement of Brownian particles driven by three different ratchet potentials: the ScI-assisted ratchet $U^*(x,t)$, the no-ScI ratchet $U_o(x,t)$, and the flashing ratchet $U_s(x,t)$. Comparing the first two ratchets reveals the effect of introducing the ScI-type auxiliary potential. The third ratchet is included to facilitate a comparison between our proposed separation scheme and a recent numerical study on ratchet-based particle separation, specifically the application of flashing ratchets for ion separation [30]. $U^*(x,t)$ and $U_o(x,t)$ follow the expressions used in Sec. III, while $U_s(x,t)$ is the same as that in Ref. [30], which is also provided in Appendix E 1. All quantities in the simulations are nondimensionalized by the same characteristic quantities $D^* = \beta = L = 1$ used in Sec. III.

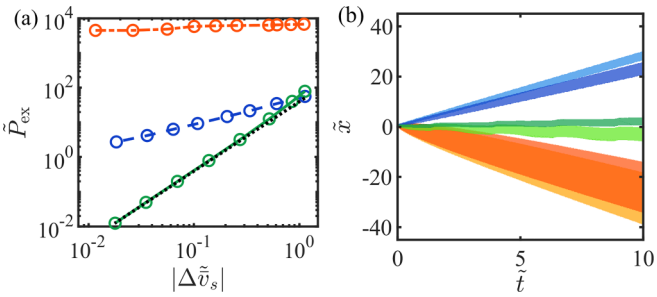

FIG. 7. Energetic costs and particle diffusion ranges at given velocity differences. (a) The total extra power required to induce given velocity differences between two particles with three ratchets. The three data series from top to bottom correspond to $U_s(x,t)$, $U_o(x,t)$, and $U^*(x,t)$. (b) The particle diffusion range represented by the average position and the associated standard deviation of the distribution. The upper two blue bands, medium two green bands, and lower two orange bands show the evolution driven by $U_o(x,t)$ ($\tilde{\tau} = 0.33$), $U^*(x,t)$ ($\tilde{\tau} = 2.5$), and $U_s(x,t)$ ($\tilde{\tau} = 0.046$). The dark and light bands represent particles with $D/D^* = 1/2$ and $D/D^* = 2$, respectively. In this plot, the driving protocol for $U_o(x,t)$ follows path II, while $U^*(x,t)$ follows the optimal path. Other parameters are the same as those used in Fig. 6.

Figure 6 shows the average velocities of two different particles at different driving speeds (magnitude of the period $\tilde{\tau}$). The results corresponding to ratchets $U^*(x,t)$, $U_o(x,t)$, and $U_s(x,t)$ are, respectively, represented by the green solid lines, blue dashed lines, and orange dash-dotted lines, where the lines with dark colors represent the particles with diffusion coefficient $D/D^* = 1/2$ and those with light colors represent the particles with $D/D^* = 2$. As illustrated in Fig. 6(a), in the slow driving regime, the no-ScI and flashing ratchets are unable to realize particle separation, while the ScI-assisted ratchet can separate the two types of particles in different directions. The two dotted lines are given by the analytical expression (8) ($\vec{j}(\vec{\lambda}) = 0$), and they agree well with the numerical results when $\tilde{\tau} \gg 1$. The independence of particle flux on the diffusion coefficient for the no-ScI ratchet and the flashing ratchet when $\tilde{\tau} \gg 1$ is demonstrated in theoretical works [40,84]. To achieve particle separation with these two conventional ratchets, the temporal period τ of the driving protocol must be significantly shorter than the particle's diffusion time $D^{*-1}L^2$, as shown in Fig. 6(b). As the period decreases, the velocities of particles driven by $U^*(x,t)$ and $U_s(x,t)$ reverse, where the reversal of particle velocities driven by $U^*(x,t)$ is visible in the inset of Fig. 6(b). The reversal driven by $U_s(x,t)$ is the key motivation for using it in particle separation [30]. Although all three ratchets demonstrate the ability to separate particles in the fast-driving regime, the velocity difference induced by the ScI-assisted ratchet is surprisingly larger than that induced by the other two conventional ratchets when $\tilde{\tau} \ll 10^{-1}$.

We further identify the working regime in which the ScI-assisted ratchet is not only solvable but also outperforms the other two ratchets, exhibiting lower energetic cost and smaller diffusion range in particle separation. The average extra power $P_{\text{ex}} \equiv W_{\text{ex}}/\tau$ required for inducing a given velocity difference between the two particles is shown in Fig. 7(a), with a detailed

algorithm provided in Appendix E 2. The energetic cost for the flashing ratchet (data linked by the orange dash-dotted line) is much higher than those for the other two continuous ratchets. The dotted line is obtained with the analytical particle flux (8) and the lower bound of (19). The ScI-assisted ratchet (data linked by the green solid line) exhibits obvious superiority in saving energy consumption in the predictable regime of $|\Delta\widetilde{\bar{v}}_s|$.

Moreover, as a stochastic system, achieving particle separation requires not only a difference in average velocity but also a distinct separation in the particles' distribution. We simulate the evolution of particles, starting from a uniform distribution in $\tilde{x} \in [0, 1]$, with three ratchets designed to induce velocity differences around $|\Delta\widetilde{\bar{v}}_s| \sim 0.5$. In Fig. 7(b), the half-width of each band represents the standard deviation of the particles' distribution, with the median value indicated by the average position of the particles. The distributions of the two types of particles driven by the ScI-assisted ratchet (the dark and light green bands in the middle) and the no-ScI ratchet (the dark and light blue bands in the upper half) are separated at $\tilde{t} = 10$. In contrast, the particles driven by the flashing ratchet (the dark and light orange bands in the lower half) are not separated, despite inducing similar velocity differences between the two particles. Compared to the no-ScI ratchet, the ScI-assisted ratchet has the advantage of reducing the device size required for observing separation.

B. Two-dimensional separation

The developed ScI-assisted ratchet can be straightforwardly generalized to higher-dimensional space to simultaneously separate more kinds of particles. We consider a two-dimensional ratchet to separate four kinds of particles, each with different diffusion coefficients: $D_1 > D_2 > D_3 > D_4$. The separation process consists of two steps. In the first step, we apply a driving force $F_x(x,t)$ in the x direction to these particles, where $F_x(x,t) = -\partial_x U_o(x,\vec{\lambda}) - \beta^{-1} D_x^{*-1} \rho_o^{-1}(x,\vec{\lambda})\dot{\vec{\lambda}} \cdot \vec{f}(x,\vec{\lambda})$ and D_x^* is a reference diffusion coefficient. The dynamic equations in this step are

$$\dot{x} = -\beta D \frac{\partial U_o(x,\vec{\lambda})}{\partial x} + \sqrt{2D}\xi_x(t) - \frac{D}{D_x^*}\frac{\dot{\vec{\lambda}} \cdot \vec{f}(x,\vec{\lambda})}{\rho_o(x,\vec{\lambda})}, \quad (29a)$$

$$\dot{y} = \sqrt{2D}\xi_y(t), \quad (29b)$$

where $\xi_x(t)$ and $\xi_y(t)$ are independent normalized Gaussian white noise. The four types of particles will be separated from left to right according to their different average velocities in the x direction: $\bar{v}_{1x} < \bar{v}_{2x} < \bar{v}_{3x} < \bar{v}_{4x}$. In the second step, once the particles with D_2 and D_3 have been largely separated, we additionally apply driving forces in the y direction on the particles. To achieve efficient separation, the particles with $D_{1,2}$ experience $F_{y\mathrm{L}}(y,t) = -\partial_y U_o(y,\vec{\lambda}) - \beta^{-1} D_{y\mathrm{L}}^{*-1} \rho_o^{-1}(y,\vec{\lambda})\dot{\vec{\lambda}} \cdot \vec{f}(y,\vec{\lambda})$ while the particles with $D_{3,4}$ experience $F_{y\mathrm{R}}(y,t) = -\partial_y U_o(y,\vec{\lambda}) - \beta^{-1} D_{y\mathrm{R}}^{*-1} \rho_o^{-1}(y,\vec{\lambda})\dot{\vec{\lambda}} \cdot \vec{f}(y,\vec{\lambda})$, where D_{yL}^* and D_{yR}^* are different reference diffusion coefficients. The dynamic equations in the second step are

$$\dot{x} = -\beta D \frac{\partial U_o(x,\vec{\lambda})}{\partial x} + \sqrt{2D}\xi_x(t) - \frac{D}{D_x^*}\frac{\dot{\vec{\lambda}} \cdot \vec{f}(x,\vec{\lambda})}{\rho_o(x,\vec{\lambda})}, \quad (30a)$$

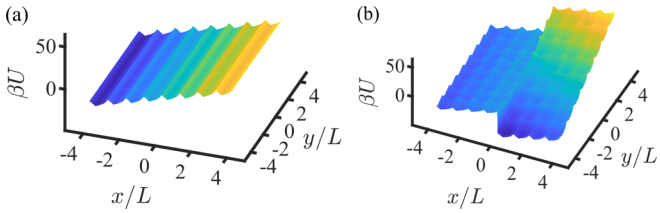

FIG. 8. The ratchet potential used for particle separation in 2D space at time $t \bmod \tau = 0.5\tau$. (a) Potential in the first step: $U(x,y,\vec{\lambda}) = U_o(x,\vec{\lambda}) + \beta^{-1} D_x^{*-1} \int_0^x \rho_o^{-1}(x',\vec{\lambda})\dot{\vec{\lambda}} \cdot \vec{f}(x',\vec{\lambda})dx'$. (b) Potential in the second step: $U(x,y,\vec{\lambda}) = U_o(x,\vec{\lambda}) + \beta^{-1} D_x^{*-1} \int_0^x \rho_o^{-1}(x',\vec{\lambda})\dot{\vec{\lambda}} \cdot \vec{f}(x',\vec{\lambda})dx' + U_o(y,\vec{\lambda}) + \beta^{-1} D_{y\mathrm{L/R}}^{*-1} \int_0^y \rho_o^{-1}(y',\vec{\lambda})\dot{\vec{\lambda}} \cdot \vec{f}(y',\vec{\lambda})dy'$.

$$\dot{y} = -\beta D \frac{\partial U_o(y,\vec{\lambda})}{\partial y} + \sqrt{2D}\xi_y(t) - D\left[\frac{\Theta(-x+\bar{v}_m t)}{D_{y\mathrm{L}}^*} + \frac{\Theta(x-\bar{v}_m t)}{D_{y\mathrm{R}}^*}\right]\frac{\dot{\vec{\lambda}} \cdot \vec{f}(y,\vec{\lambda})}{\rho_o(y,\vec{\lambda})}, \quad (30b)$$

where $\Theta(x)$ is the Heaviside step function and $\bar{v}_m$ is given by the mean value of the theoretically obtained average velocities in the x direction for D_2 and D_3. The average velocities of the particles in the y direction satisfy $\bar{v}_{1y} < \bar{v}_{2y}$ and $\bar{v}_{3y} < \bar{v}_{4y}$. Consequently, the four types of particles will be transported in different directions based on their distinct velocity vectors.

We simulate Eqs. (29a)–(30b) using the sawtooth potential illustrated in Fig. 2(a) as U_o and the driving protocol defined by $\beta\lambda_1 = 7\cos(2\pi t/\tau + \pi/6)$ and $\beta\lambda_2 = 7\sin(2\pi t/\tau + \pi/6)$. The vector function $\vec{j}(\vec{\lambda})$ is set as $j_1(\vec{\lambda}) = -\beta^2\lambda_2/30$ and $j_2(\vec{\lambda}) = \beta^2\lambda_1/30$. The corresponding potentials are illustrated in Fig. 8, and the separation results are shown in Fig. 1(b). The driving period is $\tau = 10 D_m^{-1} L^2$ and the diffusion coefficients of the particles are $D_1 = 10D_m$, $D_2 = 25D_m/7$, $D_3 = 5D_m/3$, $D_4 = D_m/5$. Additionally, $D_x^* = 2D_m$, $D_{y\mathrm{L}}^* = 25D_m/2$, and $D_{y\mathrm{R}}^* = D_m$. Here, D_m is a constant with the same dimension of diffusion coefficient, used to nondimensionalize the dynamic equations. We would like to note that while nonzero $\vec{j}(\vec{\lambda})$ typically induce particle separation in the same direction for one-dimensional systems, separation in higher dimensional systems is achieved in different directions, provided that Φ_{rev} is not negligible compared to $\oint_I d\vec{\lambda} \cdot \vec{j}(\vec{\lambda})$ in Eq. (8) and the reference diffusion coefficients for different axes are not identical.

V. DISCUSSION

We have developed a general framework that integrates thermodynamic process engineering into ratchet-based particle transport, allowing for the theoretically predictable separation of Brownian particles with different diffusion coefficients. The tractability of our approach stems from incorporating a ScI-type auxiliary potential into conventional ratchets. Specifically, for general continuously varying ratchets, we propose a designed auxiliary potential as an extension of the original ScI theory to multitype particle systems. Based

on this design, we have made several key analytical achievements: (i) We introduce a reference diffusion coefficient into the driving potential [Eq. (3)], which can be adjusted to target different separation goals. (ii) We derive a concrete expression [Eq. (8)] for the average particle flux, induced by a diffusion-coefficient-dependent effective force, facilitating particle separation in either the same or opposite directions (see Fig. 5). (iii) We determine the optimal driving protocol that minimizes energetic consumption [Eq. (19)] while maintaining a desired particle flux, utilizing the principles of thermodynamic geometry. These advancements provide a comprehensive theoretical foundation for optimizing ratchet potentials and enhancing the performance of particle separation.

As a demonstration of the effectiveness of our framework, we have compared the performance of the ScI-assisted ratchet with both the no-ScI ratchet [40] and the flashing ratchet [30] in particle separation. We have outlined operational regimes where the ScI-assisted ratchet induces a larger velocity difference and consumes less energy. This promising result encourages a systematic expansion of the comparison across a broader range of parameters. Additionally, our simulations indicate that different ratchets not only produce varying separation velocities and energy consumption but also result in different diffusion ranges. Investigating the trade-off relations between these three quantities, separation velocity, energy consumption, and diffusion range will be of significant interest [17,18]. In this paper, we deal with overdamped Brownian particles for simplicity. However, the ScI theory does not preclude the case of underdamped regimes [63,64]. It is straightforward to adapt our framework to underdamped systems, which may bring about various effects, such as negative mobility [28,85]. The impact of particle interactions also deserves attention to better model realistic separation scenarios [48,86]. Moreover, our framework holds the potential for adaptation to particle separation according to properties other than the diffusion coefficient, such as chirality [87,88] and mass [28,89].

Our analytical results of the ScI-assisted ratchet are based on the assumption of slow driving of the time-dependent parameters, where the $1/\tau$ scaling of the particle flux and energy consumption is maintained. Notably, numerical illustrations have demonstrated that this separation framework is also promising in a fast-driving regime. To explore the full behavior in the fast-driving regime, one can extend our analysis to consider the contributions from higher-order terms or directly investigate the fast-driving limit [90]. Moreover, although the framework is constructed in one-dimensional systems, we have demonstrated its capacity to simultaneously separate multitype particles in higher-dimensional systems [see Fig. 1(b)]. Given the active progress in experimental studies on ratchets [49–51] and shortcuts to isothermality [91,92], our framework could be realized and tested by integrating state-of-the-art platforms and techniques. To simplify the implementation of the ScI-assisted ratchet, the total potential may be generally expanded to take the form of an additive-multiplicative ratchet [93,94], which is feasible with current experimental advancements [95]. Ratchet implementations using optical techniques [96,97] are particularly promising since existing demonstrations of ScI have been realized with optical methods.

Currently, the combination of thermodynamic geometry and thermodynamic process control in optimizing practical thermodynamic tasks, such as heat engine optimization [98–100] and information erasure [71,101], has attracted widespread research interest. Our work extends the application scenarios in this area and lays the foundation for the innovative incorporation of thermodynamic process engineering into particle separation technology. While our framework offers a general construction, there are several challenges that remain for further extension. First, there is a need for theoretical analysis of the fast-driving regime. While the original ScI theory applies to single-type and arbitrarily fast-driven systems, we have assumed slow driving to control the motion of multitype particles simultaneously. The significant velocity variations in the fast-driving regime highlighted by numerical studies call for a systematic analysis to effectively describe very rapid separations. Furthermore, the construction of the ratchet potential may be modified based on alternative thermodynamic control strategies [61,102,103] other than ScI. Lastly, from a more general practical perspective, further attention needs to be focused on comparing the performance of different separation methods, including various ratchets and methods beyond ratchets, especially in terms of energetic significance. Choosing different separation methods in various parameter regions or combining multiple methods to achieve overall superiority might be potential ways for future optimization of particle separation.

ACKNOWLEDGMENTS

Y.H.M. thanks the National Natural Science Foundation of China for support under Grant No. 12305037 and the Fundamental Research Funds for the Central Universities under Grant No. 2023NTST017. Z.C.T. thanks the National Natural Science Foundation of China for support under Grant No. 11975050.

APPENDIX A: DERIVATION OF THE REDUCED PROBABILITY DENSITY

In the slow-driving regime, the reduced probability density is approximated as $\rho_s(x,t) = \rho_o(x,\vec{\lambda}) + \dot{\vec{\lambda}} \cdot \vec{\psi}(x,t)$, where $\vec{\psi}(x,t)$ is determined by Eq. (6). The general solution of Eq. (6) is

$$\begin{aligned}\vec{\psi}(x,t) = &\left(\frac{1}{D} - \frac{1}{D^*}\right) e^{-\beta U_o(x,\vec{\lambda})} \\ &\times \int_0^x e^{\beta U_o(x',\vec{\lambda})} [\vec{f}_o(x',\vec{\lambda}) + \vec{C}(t)] dx' \\ &+ \left(\frac{1}{D} - \frac{1}{D^*}\right) \vec{B}(t) e^{-\beta U_o(x,\vec{\lambda})}, \end{aligned} \tag{A1}$$

where $\vec{B}(t)$ is a constant of integration. From the conditions $\rho_s(0,t) = \rho_s(L,t)$, $\int_0^L \rho_s(x,t)dx = 1$ and the definition of $\rho_o(x,\vec{\lambda})$, we obtain $\vec{\psi}(0,t) = \vec{\psi}(L,t)$ and $\int_0^L \vec{\psi}(x,t)dx = 0$,

which are used to determine the expressions of $\vec{C}(t)$ and $\vec{B}(t)$:

$$\vec{C}(t) = \vec{C}(\vec{\lambda}) = -\frac{\int_0^L e^{\beta U_o(x,\vec{\lambda})}\vec{f}_o(x,\vec{\lambda})dx}{\int_0^L e^{\beta U_o(x,\vec{\lambda})}dx}, \tag{A2}$$

$$\vec{B}(t) = \vec{B}(\vec{\lambda}) = -\frac{\int_0^L e^{-\beta U_o(x,\vec{\lambda})}\int_0^x e^{\beta U_o(x',\vec{\lambda})}[\vec{f}_o(x',\vec{\lambda}) + \vec{C}(\vec{\lambda})]dx'dx}{\int_0^L e^{-\beta U_o(x,\vec{\lambda})}dx}. \tag{A3}$$

The expression of $\vec{\psi}(x,t) = \vec{\psi}(x,\vec{\lambda})$ is totally determined by $U_o(x,\vec{\lambda})$ and is independent of $\vec{j}(\vec{\lambda})$.

APPENDIX B: PARTICLE'S DIRECTED FLUX

1. Derivation of Eq. (8)

The detailed derivation of Eq. (8) is presented below. According to Eq. (7), the average probability current in a period is

$$\begin{aligned}
\bar{J}_s &\equiv \frac{1}{\tau}\int_{t_0}^{t_0+\tau} J_s(x,t)dt \\
&= \frac{1}{\tau}\int_{t_0}^{t_0+\tau}\left[-\dot{\vec{\lambda}}\cdot\vec{f}(x,\vec{\lambda}) + \left(1-\frac{D}{D^*}\right)\dot{\vec{\lambda}}\cdot\langle\vec{f}(x,\vec{\lambda})\rangle_+\right] \\
&= \frac{1}{\tau}\oint_I d\vec{\lambda}\cdot\left[-\vec{f}(x,\vec{\lambda}) + \left(1-\frac{D}{D^*}\right)\langle\vec{f}(x,\vec{\lambda})\rangle_+\right] \\
&= \frac{1}{\tau}\oint_I d\vec{\lambda}\cdot\left[-\vec{\nabla}_\lambda\int_0^x \rho_o(x',\vec{\lambda})dx' - \vec{j}(\vec{\lambda}) + \left(1-\frac{D}{D^*}\right)\frac{\int_0^L e^{\beta U_o(x,\vec{\lambda})}\vec{\nabla}_\lambda\int_0^x \rho_o(x',\vec{\lambda})dx'dx}{\int_0^L e^{\beta U_o(x,\vec{\lambda})}dx} + \left(1-\frac{D}{D^*}\right)\vec{j}(\vec{\lambda})\right] \\
&= -\frac{1}{\tau}\oint_I d\vec{\lambda}\cdot\vec{j}(\vec{\lambda}) + \frac{1}{\tau}\left(1-\frac{D}{D^*}\right)\oint_I d\vec{\lambda}\cdot\frac{\int_0^L e^{\beta U_o(x,\vec{\lambda})}\vec{\nabla}_\lambda\int_0^x \rho_o(x',\vec{\lambda})dx'dx}{\int_0^L e^{\beta U_o(x,\vec{\lambda})}dx} + \frac{1}{\tau}\left(1-\frac{D}{D^*}\right)\oint_I d\vec{\lambda}\cdot\vec{j}(\vec{\lambda}) \\
&= \frac{1}{\tau}\left(1-\frac{D}{D^*}\right)\Phi_{\rm rev} - \frac{1}{\tau}\frac{D}{D^*}\oint_I d\vec{\lambda}\cdot\vec{j}(\vec{\lambda}).
\end{aligned} \tag{B1}$$

In the above derivations, the periodicity of $\vec{\lambda}$ has been used in the third and fifth lines, the definitions of $\vec{f}(x,\vec{\lambda})$ and $\vec{f}_o(x,\vec{\lambda})$ have been used in the fourth line, and the definition of $\Phi_{\rm rev}$ has been used in the last line. The dependence of $\bar{J}_s$ on x vanishes due to the periodicity of $\vec{\lambda}$. In fact, it can be directly deduced that $\partial_x\int_{t_0}^{t_0+\tau} J_s(x,t)dt = 0$ if $\rho_s(x,t_0) = \rho_s(x,t_0+\tau)$ by integrating Eq. (1) from $t = t_0$ to $t = t_0+\tau$.

2. Expression of the effective force

The dependence of the effective force on the diffusion coefficient can be used to explain the movements of different particles in the same ratchet potential. The effective force $F_{\rm eff}$ is defined as the time-ensemble average of force $F(x,t)$, i.e., $F_{\rm eff} \equiv \tau^{-1}\int_0^\tau\int F(x,t)\rho(x,t)dx\,dt$. For particles driven by $U_o(x,\vec{\lambda}) + U_a^*(x,\vec{\lambda},\dot{\vec{\lambda}})$, $F(x,t) = -\partial_x U_o(x,\vec{\lambda}) - \partial_x U_a^*(x,\vec{\lambda},\dot{\vec{\lambda}})$, then we find

$$\begin{aligned}
F_{\rm eff} &= \frac{1}{\tau}\int_0^\tau\int\left[-\frac{\partial U_o(x,\vec{\lambda})}{\partial x} - \frac{\partial U_a^*(x,\vec{\lambda},\dot{\vec{\lambda}})}{\partial x}\right]\rho(x,t)dx\,dt \\
&= \frac{1}{\tau}\int_0^\tau\int\frac{1}{\beta}\left(\frac{1}{D}J(x,t) + \frac{\partial\rho(x,t)}{\partial x}\right)dx\,dt \\
&= \frac{1}{\tau}\frac{1}{\beta D}\int_0^\tau\int J(x,t)dx\,dt \\
&= \frac{1}{\tau}\frac{1}{\beta D}\int_0^\tau\int_0^L J_s(x,t)dx\,dt \\
&= \frac{1}{\beta D}\int_0^L \bar{J}_s dx = \frac{\bar{v}_s}{\beta D} = \frac{L}{\beta\tau}\left(\frac{1}{D}-\frac{1}{D^*}\right)\Phi_{\rm rev} \\
&\quad - \frac{L}{\beta\tau}\frac{1}{D^*}\oint_I d\vec{\lambda}\cdot\vec{j}(\vec{\lambda}).
\end{aligned} \tag{B2}$$

In the above derivation, we have used the definitions of $J(x,t)$, $J_s(x,t)$, $\bar{v}_s$, and the fact that $\rho(x,t)$ vanishes at infinity. The direction of $F_{\rm eff}$ is consistent with the direction of the average velocity $\bar{v}_s$, depending on the values of D.

3. Necessity of asymmetric potentials for nonzero $\Phi_{\rm rev}$

According to Eq. (9), the reversible integrated flow $\Phi_{\rm rev}$ reads

$$\Phi_{\rm rev} = \oint_I d\vec{\lambda}\cdot\frac{\int_0^L e^{\beta U_o(x,\vec{\lambda})}\vec{f}_o(x,\vec{\lambda})dx}{\int_0^L e^{\beta U_o(x,\vec{\lambda})}dx}. \tag{B3}$$

If the potential $U_o(x,\vec{\lambda})$ is symmetric, namely, there is always a reference axis to make $U_o(x,\vec{\lambda}) = U_o(-x,\vec{\lambda})$ for any x, then $\rho_o(x,\vec{\lambda}) = \rho_o(-x,\vec{\lambda})$ and $\vec{f}_o(x,\vec{\lambda}) = -\vec{f}_o(-x,\vec{\lambda})$.

Defining $y = -x$, one has

$$\Phi_{\rm rev} = \oint_I d\vec{\lambda} \cdot \frac{-\int_0^L e^{\beta U_o(-y,\vec{\lambda})} \vec{f}_o(-y,\vec{\lambda}) dy}{-\int_0^L e^{\beta U_o(-y,\vec{\lambda})} dy} = \oint_I d\vec{\lambda} \cdot \frac{-\int_0^L e^{\beta U_o(y,\vec{\lambda})} \vec{f}_o(y,\vec{\lambda}) dy}{\int_0^L e^{\beta U_o(y,\vec{\lambda})} dy} = -\Phi_{\rm rev}, \quad \text{(B4)}$$

which obviously indicates $\Phi_{\rm rev} = 0$. Hence, an asymmetric $U_o(x,\vec{\lambda})$ is needed to generate nonzero $\Phi_{\rm rev}$.

APPENDIX C: DERIVATIONS OF ENERGETIC QUANTITIES

1. Derivations of the internal energy and its variation

Substituting the total potential (10) into the definition of internal energy, we have

$$\begin{aligned} E(t) &= \int U^*(x,t)\rho(x,t)dx \\ &= \int V^*(x,t)\rho(x,t)dx + \frac{\varepsilon^*(t)}{L}\int x\rho(x,t)dx \\ &= \sum_{n\in\mathbb{Z}} \int_{nL}^{(n+1)L} V^*(x,t)\rho(x,t)dx + \frac{\varepsilon^*(t)}{L}\langle x\rangle_t \\ &= \sum_{n\in\mathbb{Z}} \int_0^L V^*(x'+nL,t)\rho(x'+nL,t)dx' + \frac{\varepsilon^*(t)}{L}\langle x\rangle_t \\ &= \sum_{n\in\mathbb{Z}} \int_0^L V^*(x',t)\rho(x'+nL,t)dx' + \frac{\varepsilon^*(t)}{L}\langle x\rangle_t \\ &= \int_0^L V^*(x',t)\sum_{n\in\mathbb{Z}}\rho(x'+nL,t)dx' + \frac{\varepsilon^*(t)}{L}\langle x\rangle_t \\ &= \int_0^L V^*(x,t)\rho_s(x,t)dx + \frac{\varepsilon^*(t)}{L}\langle x\rangle_t, \end{aligned} \quad \text{(C1)}$$

where the spatial periodicity of $V^*(x,t)$ and the definition of $\rho_s(x,t)$ have been used. $\langle x\rangle_t \equiv \int x\rho(x,t)dx$ is the ensemble-averaged position of the particles at time t.

Considering that the first term in $E(t)$ as well as $\varepsilon^*(t)$ are temporally periodic, the variation of $E(t)$ from $t = t_0$ to $t = t_0 + \tau$ is

$$\begin{aligned} \Delta E &= \frac{\varepsilon^*(t_0)}{L}\bar{v}_s\tau = \varepsilon^*(t_0)\bar{J}_s\tau \\ &= \varepsilon^*(t_0)\left[\left(1-\frac{D}{D^*}\right)\Phi_{\rm rev} - \frac{D}{D^*}\oint_I d\vec{\lambda}\cdot\vec{j}(\vec{\lambda})\right], \end{aligned} \quad \text{(C2)}$$

which becomes more compact as Eq. (14) by setting $\vec{j}(\vec{\lambda}) = 0$.

2. Derivation of ensemble-averaged heat absorption

The ensemble-averaged heat current is

$$\begin{aligned} \dot{Q} &= \int U^*(x,t)\frac{\partial\rho(x,t)}{\partial t}dx \\ &= -\int U^*(x,t)\frac{\partial J(x,t)}{\partial x}dx \\ &= -U^*(x,t)J(x,t)\Big|_{-\infty}^{+\infty} - \int F(x,t)J(x,t)dx \\ &= -\sum_{n\in\mathbb{Z}}\int_{nL}^{(n+1)L} F(x,t)J(x,t)dx \\ &= -\sum_{n\in\mathbb{Z}}\int_0^L F(x+nL,t)J(x+nL,t)dx \\ &= -\int_0^L F(x,t)J_s(x,t)dx \\ &= \int_0^L \left[\frac{\partial U_o(x,\vec{\lambda})}{\partial x} + \frac{\partial U_a^*(x,t)}{\partial x}\right]J_s(x,t)dx, \end{aligned} \quad \text{(C3)}$$

where $F(x,t) \equiv -\partial_x U^*(x,t)$ and $J_s(x,t)$ is the reduced probability current. In the above derivation, we have used the fact that the physical current $J(x,t)$ vanishes at infinity and the spatial periodicity of $F(x,t)$. Substituting the expressions of $\partial_x U^*(x,t)$ and $J_s(x,t)$ into the above equation, we obtain

$$\begin{aligned} \dot{Q} &= \int_0^L \left[\frac{\partial U_o(x,\vec{\lambda})}{\partial x} + \frac{1}{\beta D^*}\frac{\dot{\vec{\lambda}}\cdot\vec{f}(x,\vec{\lambda})}{\rho_o(x,\vec{\lambda})}\right]\left[-\dot{\vec{\lambda}}\cdot\vec{f}(x,\vec{\lambda}) + \left(1-\frac{D}{D^*}\right)\dot{\vec{\lambda}}\cdot\langle\vec{f}(x,\vec{\lambda})\rangle_+\right]dx \\ &= -\int_0^L \frac{\partial U_o(x,\vec{\lambda})}{\partial x}\dot{\vec{\lambda}}\cdot\vec{f}(x,\vec{\lambda})dx + \left(1-\frac{D}{D^*}\right)\dot{\vec{\lambda}}\cdot\langle\vec{f}(x,\vec{\lambda})\rangle_+\int_0^L\frac{\partial U_o(x,\vec{\lambda})}{\partial x}dx \\ &\quad - \frac{1}{\beta D^*}\int_0^L\frac{[\dot{\vec{\lambda}}\cdot\vec{f}(x,\vec{\lambda})]^2}{\rho_o(x,\vec{\lambda})}dx + \frac{1}{\beta D^*}\left(1-\frac{D}{D^*}\right)\dot{\vec{\lambda}}\cdot\langle\vec{f}(x,\vec{\lambda})\rangle_+\int_0^L\frac{\dot{\vec{\lambda}}\cdot\vec{f}(x,\vec{\lambda})}{\rho_o(x,\vec{\lambda})}dx \\ &= -\int_0^L\frac{\partial U_o(x,\vec{\lambda})}{\partial x}\dot{\vec{\lambda}}\cdot\left[\int_0^x\vec{\nabla}_\lambda\rho_o(x',\vec{\lambda})dx'\right]dx - \dot{\vec{\lambda}}\cdot\vec{j}(\vec{\lambda})\int_0^L\frac{\partial U_o(x,\vec{\lambda})}{\partial x}dx + 0 \\ &\quad - \frac{1}{\beta D^*}Z_-(\vec{\lambda})Z_+(\vec{\lambda})\langle[\dot{\vec{\lambda}}\cdot\vec{f}(x,\vec{\lambda})]^2\rangle_+ + \frac{1}{\beta D^*}\left(1-\frac{D}{D^*}\right)Z_-(\vec{\lambda})Z_+(\vec{\lambda})[\dot{\vec{\lambda}}\cdot\langle\vec{f}(x,\vec{\lambda})\rangle_+]^2 \\ &= -\left[U_o(x,\vec{\lambda})\dot{\vec{\lambda}}\cdot\int_0^x\vec{\nabla}_\lambda\rho_o(x',\vec{\lambda})dx'\right]\Big|_0^L + \int_0^L U_o(x,\vec{\lambda})\dot{\vec{\lambda}}\cdot\vec{\nabla}_\lambda\rho_o(x,\vec{\lambda})dx - 0 \end{aligned}$$

$$
\begin{aligned}
&- \frac{1}{\beta D^*} Z_-(\vec{\lambda}) Z_+(\vec{\lambda}) \langle [\dot{\vec{\lambda}} \cdot \vec{f}(x, \vec{\lambda})]^2 \rangle_+ + \frac{1}{\beta D^*} \left(1 - \frac{D}{D^*}\right) Z_-(\vec{\lambda}) Z_+(\vec{\lambda}) [\langle \dot{\vec{\lambda}} \cdot \vec{f}(x, \vec{\lambda}) \rangle_+]^2 \\
&= 0 + \dot{\vec{\lambda}} \cdot \vec{\nabla}_\lambda \int_0^L U_o(x, \vec{\lambda}) \rho_o(x, \vec{\lambda}) dx - \dot{\vec{\lambda}} \cdot \int_0^L [\vec{\nabla}_\lambda U_o(x, \vec{\lambda})] \rho_o(x, \vec{\lambda}) dx \\
&\quad - \frac{1}{\beta D^*} Z_-(\vec{\lambda}) Z_+(\vec{\lambda}) \langle [\dot{\vec{\lambda}} \cdot \vec{f}(x, \vec{\lambda})]^2 \rangle_+ + \frac{1}{\beta D^*} \left(1 - \frac{D}{D^*}\right) Z_-(\vec{\lambda}) Z_+(\vec{\lambda}) [\langle \dot{\vec{\lambda}} \cdot \vec{f}(x, \vec{\lambda}) \rangle_+]^2 \\
&= \dot{\vec{\lambda}} \cdot \vec{\nabla}_\lambda \int_0^L U_o(x, \vec{\lambda}) \rho_o(x, \vec{\lambda}) dx + \frac{1}{\beta} \dot{\vec{\lambda}} \cdot \vec{\nabla}_\lambda \ln Z_- \\
&\quad - \frac{1}{\beta D^*} Z_-(\vec{\lambda}) Z_+(\vec{\lambda}) \langle [\dot{\vec{\lambda}} \cdot \vec{f}(x, \vec{\lambda})]^2 \rangle_+ + \frac{1}{\beta D^*} \left(1 - \frac{D}{D^*}\right) Z_-(\vec{\lambda}) Z_+(\vec{\lambda}) [\langle \dot{\vec{\lambda}} \cdot \vec{f}(x, \vec{\lambda}) \rangle_+]^2. \qquad \text{(C4)}
\end{aligned}
$$

Then, the heat absorbed by the particle in a temporal period is

$$
\begin{aligned}
Q &= \int_{t_0}^{t_0+\tau} \dot{Q} dt \\
&= \oint_I d\vec{\lambda} \cdot \vec{\nabla}_\lambda \left\{ \int_0^L U_o(x, \vec{\lambda}) \rho_o(x, \vec{\lambda}) dx + \frac{1}{\beta} \ln Z_- \right\} \\
&\quad - \frac{1}{\beta D^*} \int_{t_0}^{t_0+\tau} dt \left\{ Z_-(\vec{\lambda}) Z_+(\vec{\lambda}) \langle [\dot{\vec{\lambda}} \cdot \vec{f}(x, \vec{\lambda})]^2 \rangle_+ - \left(1 - \frac{D}{D^*}\right) Z_-(\vec{\lambda}) Z_+(\vec{\lambda}) [\langle \dot{\vec{\lambda}} \cdot \vec{f}(x, \vec{\lambda}) \rangle_+]^2 \right\} \\
&= 0 - \frac{1}{\beta D^*} \int_{t_0}^{t_0+\tau} dt Z_-(\vec{\lambda}) Z_+(\vec{\lambda}) \left\{ \langle [\dot{\vec{\lambda}} \cdot \vec{f}(x, \vec{\lambda})]^2 \rangle_+ - \left(1 - \frac{D}{D^*}\right) [\langle \dot{\vec{\lambda}} \cdot \vec{f}(x, \vec{\lambda}) \rangle_+]^2 \right\} \\
&= - \int_{t_0}^{t_0+\tau} dt \dot{\lambda}_\alpha \dot{\lambda}_\beta \frac{1}{\beta D^*} Z_-(\vec{\lambda}) Z_+(\vec{\lambda}) \left\{ \langle f_\alpha(x, \vec{\lambda}) f_\beta(x, \vec{\lambda}) \rangle_+ - \left(1 - \frac{D}{D^*}\right) \langle f_\alpha(x, \vec{\lambda}) \rangle_+ \langle f_\beta(x, \vec{\lambda}) \rangle_+ \right\} \\
&\equiv - \int_{t_0}^{t_0+\tau} dt \dot{\lambda}_\alpha \dot{\lambda}_\beta G_{\alpha\beta}(\vec{\lambda}), \qquad \text{(C5)}
\end{aligned}
$$

where we have used the condition that the driving trajectory in the parametric space is a loop.

3. The positive semidefiniteness of $G_{\alpha\beta}(\vec{\lambda})$

In the following, we present a proof that $G_{\alpha\beta}(\vec{\lambda})$ is a positive semidefinite matrix. First, $G_{\alpha\beta}(\vec{\lambda}) = G_{\beta\alpha}(\vec{\lambda})$ by definition. Second, for any N-dimensional vector $\vec{v} = (v_1, v_2, \ldots, v_N)$, we have

$$
\begin{aligned}
\vec{v} G(\vec{\lambda}) \vec{v}^T &= v_\alpha G_{\alpha\beta}(\vec{\lambda}) v_\beta \\
&= v_\alpha \frac{1}{\beta D^*} Z_-(\vec{\lambda}) Z_+(\vec{\lambda}) \left\{ \langle f_\alpha(x, \vec{\lambda}) f_\beta(x, \vec{\lambda}) \rangle_+ - \left(1 - \frac{D}{D^*}\right) \langle f_\alpha(x, \vec{\lambda}) \rangle_+ \langle f_\beta(x, \vec{\lambda}) \rangle_+ \right\} v_\beta \\
&= \frac{1}{\beta D^*} Z_-(\vec{\lambda}) Z_+(\vec{\lambda}) \left\{ \langle [\vec{v} \cdot \vec{f}(x, \vec{\lambda})]^2 \rangle_+ - \left(1 - \frac{D}{D^*}\right) [\langle \vec{v} \cdot \vec{f}(x, \vec{\lambda}) \rangle_+]^2 \right\} \\
&\geqslant \frac{1}{\beta D^*} Z_-(\vec{\lambda}) Z_+(\vec{\lambda}) \left\{ [\langle \vec{v} \cdot \vec{f}(x, \vec{\lambda}) \rangle_+]^2 - \left(1 - \frac{D}{D^*}\right) [\langle \vec{v} \cdot \vec{f}(x, \vec{\lambda}) \rangle_+]^2 \right\} \\
&= \frac{1}{\beta D^*} Z_-(\vec{\lambda}) Z_+(\vec{\lambda}) \left\{ \frac{D}{D^*} [\langle \vec{v} \cdot \vec{f}(x, \vec{\lambda}) \rangle_+]^2 \right\} \\
&\geqslant 0, \qquad \text{(C6)}
\end{aligned}
$$

where the inequality $\langle [\vec{v} \cdot \vec{f}(x, \vec{\lambda})]^2 \rangle_+ \geqslant [\langle \vec{v} \cdot \vec{f}(x, \vec{\lambda}) \rangle_+]^2$ is obtained via the Cauchy-Schwarz inequality. Here, the inner product of functions M and N is defined as

$$
\langle M, N \rangle \equiv \langle MN \rangle_+ = \frac{\int_0^L e^{\beta U_o(x, \vec{\lambda})} MN dx}{\int_0^L e^{\beta U_o(x, \vec{\lambda})} dx}. \qquad \text{(C7)}
$$

Therefore, $G_{\alpha\beta}(\vec{\lambda})$ is positive semidefinite and $Q \leqslant 0$.

4. The lower bound of work cost

Using the Cauchy-Schwarz inequality, one derives the lower bound of work cost in a temporal period on given driving loop as follows:

$$\begin{aligned} W &= \Delta E - Q = \Delta E + \int_{t_0}^{t_0+\tau} dt \dot{\lambda}_\alpha \dot{\lambda}_\beta G_{\alpha\beta}(\vec{\lambda}) \\ &\geqslant \Delta E + \frac{1}{\tau}\left[\int_{t_0}^{t_0+\tau} dt \sqrt{\dot{\lambda}_\alpha \dot{\lambda}_\beta G_{\alpha\beta}(\vec{\lambda})}\right]^2 \\ &= \Delta E + \frac{\mathcal{L}^2}{\tau} = \Delta E + \frac{D^* \mathcal{L}^2 \bar{J}_s}{(D^* - D)\Phi_{\text{rev}} - D \oint_I d\vec{\lambda} \cdot \vec{j}(\vec{\lambda})}, \end{aligned} \tag{C8}$$

which turns out to be Eq. (19) when $\vec{j}(\vec{\lambda}) = 0$. We have used Eq. (8) in the last line of the above derivation. The equality in the above expression is achieved when the driving dynamics satisfies $\sqrt{\dot{\lambda}_\alpha \dot{\lambda}_\beta G_{\alpha\beta}(\vec{\lambda})} = \text{const}$. We do not consider the effect of the driving dynamics on ΔE, as the average value of this quantity over the initial moment taking from 0 to τ is a geometric quantity,

$$\begin{aligned} \overline{\Delta E} &\equiv \frac{1}{\tau}\int_0^\tau dt_0 [E(t_0+\tau) - E(t_0)] \\ &= \frac{1}{\tau}\left[\int_0^\tau dt_0 \varepsilon^*(t_0)\right]\left[\left(1 - \frac{D}{D^*}\right)\Phi_{\text{rev}} - \frac{D}{D^*}\oint_I d\vec{\lambda} \cdot \vec{j}(\vec{\lambda})\right] \\ &= \frac{1}{\beta D^* \tau}\left[\oint_I d\vec{\lambda} \cdot Z_-(\vec{\lambda}) Z_+(\vec{\lambda}) \langle \vec{f}(x, \vec{\lambda})\rangle_+\right]\left[\Phi_{\text{rev}} - \frac{D}{D^*}\oint_I d\vec{\lambda} \cdot \langle \vec{f}(x, \vec{\lambda})\rangle_+\right], \end{aligned} \tag{C9}$$

which is independent of the driving protocol for a given driving loop.

APPENDIX D: ILLUSTRATION DETAILS

1. Calculate the specific expression of the auxiliary potential

To obtain the expression of the auxiliary potential, according to Eq. (3), we need to calculate $Z_-(\vec{\lambda})$, $\rho_o(x, \vec{\lambda})$ and $\vec{f}_o(x, \vec{\lambda})$. First, according to Eq. (21), $Z_-(\vec{\lambda})$ is specifically obtained as

$$Z_-(\vec{\lambda}) \equiv \int_0^L e^{-\beta U_o(x,\vec{\lambda})} dx = -\frac{\alpha L}{\beta}\frac{e^{-\beta\lambda_1} - 1}{\lambda_1} - \frac{L - 2\alpha L}{\beta}\frac{e^{-\beta\lambda_2} - e^{-\beta\lambda_1}}{\lambda_2 - \lambda_1} + \frac{\alpha L}{\beta}\frac{1 - e^{-\beta\lambda_2}}{\lambda_2}, \tag{D1}$$

which further gives

$$\frac{\partial Z_-}{\partial \lambda_1} = -\frac{\alpha L}{\beta}\frac{-\beta\lambda_1 e^{-\beta\lambda_1} - e^{-\beta\lambda_1} + 1}{\lambda_1^2} - \frac{L - 2\alpha L}{\beta}\frac{\beta(\lambda_2 - \lambda_1)e^{-\beta\lambda_1} + e^{-\beta\lambda_2} - e^{-\beta\lambda_1}}{(\lambda_2 - \lambda_1)^2}, \tag{D2}$$

$$\frac{\partial Z_-}{\partial \lambda_2} = \frac{L - 2\alpha L}{\beta}\frac{\beta(\lambda_2 - \lambda_1)e^{-\beta\lambda_2} + e^{-\beta\lambda_2} - e^{-\beta\lambda_1}}{(\lambda_2 - \lambda_1)^2} + \frac{\alpha L}{\beta}\frac{\beta\lambda_2 e^{-\beta\lambda_2} - 1 + e^{-\beta\lambda_2}}{\lambda_2^2}, \tag{D3}$$

and

$$\rho_o(x, \vec{\lambda}) \equiv \frac{e^{-\beta U_o(x,\vec{\lambda})}}{Z_-(\vec{\lambda})} = \begin{cases} \frac{1}{Z_-(\vec{\lambda})} e^{-\beta\lambda_1 \frac{x}{\alpha L}}, & 0 \leqslant x \leqslant \alpha L \\ \frac{1}{Z_-(\vec{\lambda})} e^{-\beta[\lambda_1 \frac{L-x-\alpha L}{L-2\alpha L} + \lambda_2 \frac{x-\alpha L}{L-2\alpha L}]}, & \alpha L < x \leqslant L - \alpha L \\ \frac{1}{Z_-(\vec{\lambda})} e^{-\beta\lambda_2 \frac{L-x}{\alpha L}}, & L - \alpha L < x \leqslant L. \end{cases} \tag{D4}$$

For $0 < x \leqslant \alpha L$, the first and second components of $\vec{f}_o(x, \vec{\lambda})$ are, respectively,

$$f_{o1}(x, \vec{\lambda}) \equiv \int_0^x \frac{\partial \rho_o(x', \vec{\lambda})}{\partial \lambda_1} dx' = -\frac{1}{Z_-(\vec{\lambda})}\frac{1}{\beta\lambda_1^2}\left[\alpha L - (\alpha L + \beta\lambda_1 x)e^{-\beta\lambda_1 \frac{x}{\alpha L}}\right] - \frac{1}{Z_-^2(\vec{\lambda})}\frac{\partial Z_-}{\partial \lambda_1}\frac{\alpha L}{\beta\lambda_1}\left(1 - e^{-\beta\lambda_1 \frac{x}{\alpha L}}\right) \tag{D5}$$

and

$$f_{o2}(x, \vec{\lambda}) \equiv \int_0^x \frac{\partial \rho_o(x', \vec{\lambda})}{\partial \lambda_2} dx' = -\frac{1}{Z_-^2(\vec{\lambda})}\frac{\partial Z_-}{\partial \lambda_2}\frac{\alpha L}{\beta\lambda_1}\left(1 - e^{-\beta\lambda_1 \frac{x}{\alpha L}}\right). \tag{D6}$$

For $\alpha L < x \leqslant L - \alpha L$,

$$
\begin{aligned}
f_{o1}(x,\vec{\lambda}) &= \int_0^{\alpha L} \frac{\partial \rho_o(x,\vec{\lambda})}{\partial \lambda_1} dx + \int_{\alpha L}^{x} \frac{\partial \rho_o(x',\vec{\lambda})}{\partial \lambda_1} dx' \\
&= -\frac{1}{Z_-(\vec{\lambda})} \frac{\alpha L}{\beta \lambda_1^2} [1 - (1+\beta\lambda_1) e^{-\beta\lambda_1}] - \frac{1}{Z_-^2(\vec{\lambda})} \frac{\partial Z_-}{\partial \lambda_1} \frac{\alpha L}{\beta \lambda_1} (1 - e^{-\beta\lambda_1}) - \beta \frac{1}{Z_-(\vec{\lambda})} \frac{1}{\beta^2(\lambda_1-\lambda_2)^2} [1 + \beta(\lambda_1 - \lambda_2)] \\
&\quad \times (2\alpha L - L) e^{-\beta\lambda_1} - \beta \frac{1}{Z_-(\vec{\lambda})} \frac{1}{\beta^2(\lambda_1-\lambda_2)^2} [L - 2\alpha L - \alpha L \beta(\lambda_1-\lambda_2) + \beta(\lambda_1-\lambda_2)(L-x)] e^{-\beta\left(\frac{L-x-\alpha L}{L-2\alpha L}\lambda_1 + \frac{x-\alpha L}{L-2\alpha L}\lambda_2\right)} \\
&\quad - \frac{1}{Z_-^2(\vec{\lambda})} \frac{\partial Z_-}{\partial \lambda_1} \frac{L - 2\alpha L}{\beta(\lambda_1-\lambda_2)} \left[e^{-\beta \frac{\lambda_1 L - (\lambda_1-\lambda_2)x - (\lambda_1+\lambda_2)\alpha L}{L-2\alpha L}} - e^{-\beta\lambda_1} \right],
\end{aligned} \tag{D7}
$$

$$
\begin{aligned}
f_{o2}(x,\vec{\lambda}) &= \int_0^{\alpha L} \frac{\partial \rho_o(x,\vec{\lambda})}{\partial \lambda_2} dx + \int_{\alpha L}^{x} \frac{\partial \rho_o(x',\vec{\lambda})}{\partial \lambda_2} dx' \\
&= -\frac{1}{Z_-^2(\vec{\lambda})} \frac{\partial Z_-}{\partial \lambda_2} \frac{\alpha L}{\beta \lambda_1} (1 - e^{-\beta\lambda_1}) \\
&\quad - \frac{\beta}{Z_-(\vec{\lambda})} \frac{1}{\beta^2(\lambda_1-\lambda_2)^2} \left\{ (L - 2\alpha L) e^{-\beta\lambda_1} - [L - 2\alpha L + \alpha L \beta(\lambda_1-\lambda_2) - \beta(\lambda_1-\lambda_2)x] e^{-\beta\left(\frac{L-\alpha L-x}{L-2\alpha L}\lambda_1 + \frac{x-\alpha L}{L-2\alpha L}\lambda_2\right)} \right\} \\
&\quad - \frac{1}{Z_-^2(\vec{\lambda})} \frac{\partial Z_-}{\partial \lambda_2} \frac{L - 2\alpha L}{\beta(\lambda_1-\lambda_2)} \left[e^{-\beta \frac{\lambda_1 L - (\lambda_1-\lambda_2)x - (\lambda_1+\lambda_2)\alpha L}{L-2\alpha L}} - e^{-\beta\lambda_1} \right].
\end{aligned} \tag{D8}
$$

For $L - \alpha L < x \leqslant L$,

$$
\begin{aligned}
f_{o1}(x,\vec{\lambda}) &= \int_0^{\alpha L} \frac{\partial \rho_o(x,\vec{\lambda})}{\partial \lambda_1} dx + \int_{\alpha L}^{L-\alpha L} \frac{\partial \rho_o(x,\vec{\lambda})}{\partial \lambda_1} dx + \int_{L-\alpha L}^{x} \frac{\partial \rho_o(x',\vec{\lambda})}{\partial \lambda_1} dx' \\
&= -\frac{1}{Z_-(\vec{\lambda})} \frac{\alpha L}{\beta \lambda_1^2} \left[1 - (1+\beta\lambda_1) e^{-\beta\lambda_1} \right] - \frac{1}{Z_-^2(\vec{\lambda})} \frac{\partial Z_-}{\partial \lambda_1} \frac{\alpha L}{\beta \lambda_1} (1 - e^{-\beta\lambda_1}) \\
&\quad - \beta \frac{1}{Z_-(\vec{\lambda})} \frac{1}{\beta^2(\lambda_1-\lambda_2)^2} \left\{ [1 + \beta(\lambda_1-\lambda_2)](2\alpha L - L) e^{-\beta\lambda_1} + (L - 2\alpha L) e^{-\beta\lambda_2} \right\} \\
&\quad - \frac{1}{Z_-^2(\vec{\lambda})} \frac{\partial Z_-}{\partial \lambda_1} \frac{L - 2\alpha L}{\beta(\lambda_1-\lambda_2)} (e^{-\beta\lambda_2} - e^{-\beta\lambda_1}) - \frac{1}{Z_-^2(\vec{\lambda})} \frac{\partial Z_-}{\partial \lambda_1} \frac{\alpha L}{\beta \lambda_2} \left(e^{-\beta\lambda_2 \frac{L-x}{\alpha L}} - e^{-\beta\lambda_2} \right),
\end{aligned} \tag{D9}
$$

$$
\begin{aligned}
f_{o2}(x,\vec{\lambda}) &= \int_0^{\alpha L} \frac{\partial \rho_o(x,\vec{\lambda})}{\partial \lambda_2} dx + \int_{\alpha L}^{L-\alpha L} \frac{\partial \rho_o(x,\vec{\lambda})}{\partial \lambda_2} dx + \int_{L-\alpha L}^{x} \frac{\partial \rho_o(x',\vec{\lambda})}{\partial \lambda_2} dx' \\
&= -\frac{1}{Z_-^2(\vec{\lambda})} \frac{\partial Z_-}{\partial \lambda_2} \frac{\alpha L}{\beta \lambda_1} (1 - e^{-\beta\lambda_1}) - \frac{\beta}{Z_-(\vec{\lambda})} \frac{1}{\beta^2(\lambda_1-\lambda_2)^2} \{ (L - 2\alpha L) e^{-\beta\lambda_1} - (L - 2\alpha L)[1 - \beta(\lambda_1-\lambda_2)] e^{-\beta\lambda_2} \} \\
&\quad - \frac{1}{Z_-^2(\vec{\lambda})} \frac{\partial Z_-}{\partial \lambda_2} \frac{L - 2\alpha L}{\beta(\lambda_1-\lambda_2)} (e^{-\beta\lambda_2} - e^{-\beta\lambda_1}) - \beta \frac{1}{Z_-(\vec{\lambda})} \frac{1}{\beta^2 \lambda_2^2} \left\{ [\alpha L + (L-x)\beta\lambda_2] e^{-\beta\lambda_2 \frac{L-x}{\alpha L}} - \alpha L (1 + \beta\lambda_2) e^{-\beta\lambda_2} \right\} \\
&\quad - \frac{1}{Z_-^2(\vec{\lambda})} \frac{\partial Z_-}{\partial \lambda_2} \frac{\alpha L}{\beta \lambda_2} \left(e^{-\beta\lambda_2 \frac{L-x}{\alpha L}} - e^{-\beta\lambda_2} \right).
\end{aligned} \tag{D10}
$$

The expression of $U_a^*(x,\vec{\lambda},\dot{\vec{\lambda}})$ is consistently obtained by integrating $\partial x U_a^*(x,\vec{\lambda},\dot{\vec{\lambda}}) = \beta^{-1} D^{*-1} \rho_o^{-1}(x,\vec{\lambda}) \dot{\vec{\lambda}} \cdot [\vec{f}_o(x,\vec{\lambda}) + \vec{j}(\vec{\lambda})]$, with given expression of $\vec{j}(\vec{\lambda})$.

2. Determine the parameters of the sawtooth potential

The values of $(\partial_{\lambda_2} C_1 - \partial_{\lambda_1} C_2)$ on the parametric space and Φ_{rev} as a function of α are shown in Fig. 9.

3. Illustration of steady periodic evolution

It is demonstrated by simulations that in the slow-driving regime, the analytical probability density $\rho_s(x,t) = \rho_o(x,\vec{\lambda}) + \dot{\vec{\lambda}} \cdot \vec{\psi}(x,\vec{\lambda})$ is consistent with the reduced distribution of the Brownian particles when they enter the steady periodic state. Simulate the evolution of the particles with Eq. (24), where U_o is expressed as Eq. (21) and $\vec{j}(\vec{\lambda}) = 0$. The driving loop is $\beta\lambda_1 = \beta R \cos(2\pi f(s) + \theta_0)$ and $\beta\lambda_2 = \beta R \sin(2\pi f(s) + \theta_0)$, where $s \equiv t/\tau$, $\theta_0 = \pi/6$ and $\beta R = 7$. Beginning with a uniform distribution on $x \in [0, L]$, the particles enter the steady state after several driving periods, i.e., their reduced probability distribution on $[0, L]$ is periodic. Figures 10(a) and 10(b) show the evolution of the

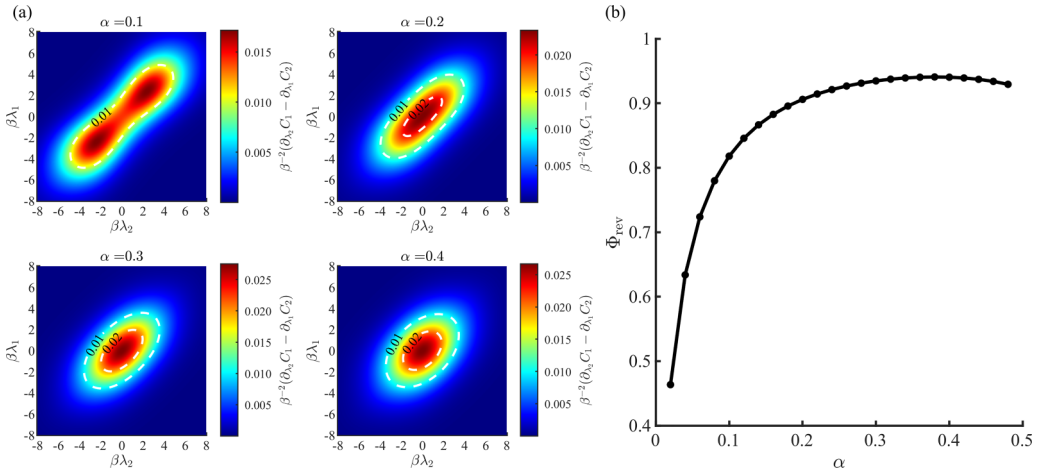

FIG. 9. (a) The value of $(\partial_{\lambda_2} C_1 - \partial_{\lambda_1} C_2)$ on the parametric space. (b) Φ_{rev} as a function of α where the driving loop is a circle with $\beta R = 7$.

steady-state distribution under the protocol along paths II and III defined in Sec. III, respectively. The normalized histograms in the upper panels of Figs. 10(a) and 10(b) represent the actual distributions $\rho(x,t)\Delta x$ at different times and those in the lower panels represent the corresponding reduced distributions $\rho_s(x,t)\Delta x \equiv \sum_{n\in\mathbb{Z}} \rho(x+nL,t)\Delta x$. The analytical predictions (red lines in the lower panels) coincide well with the simulation results.

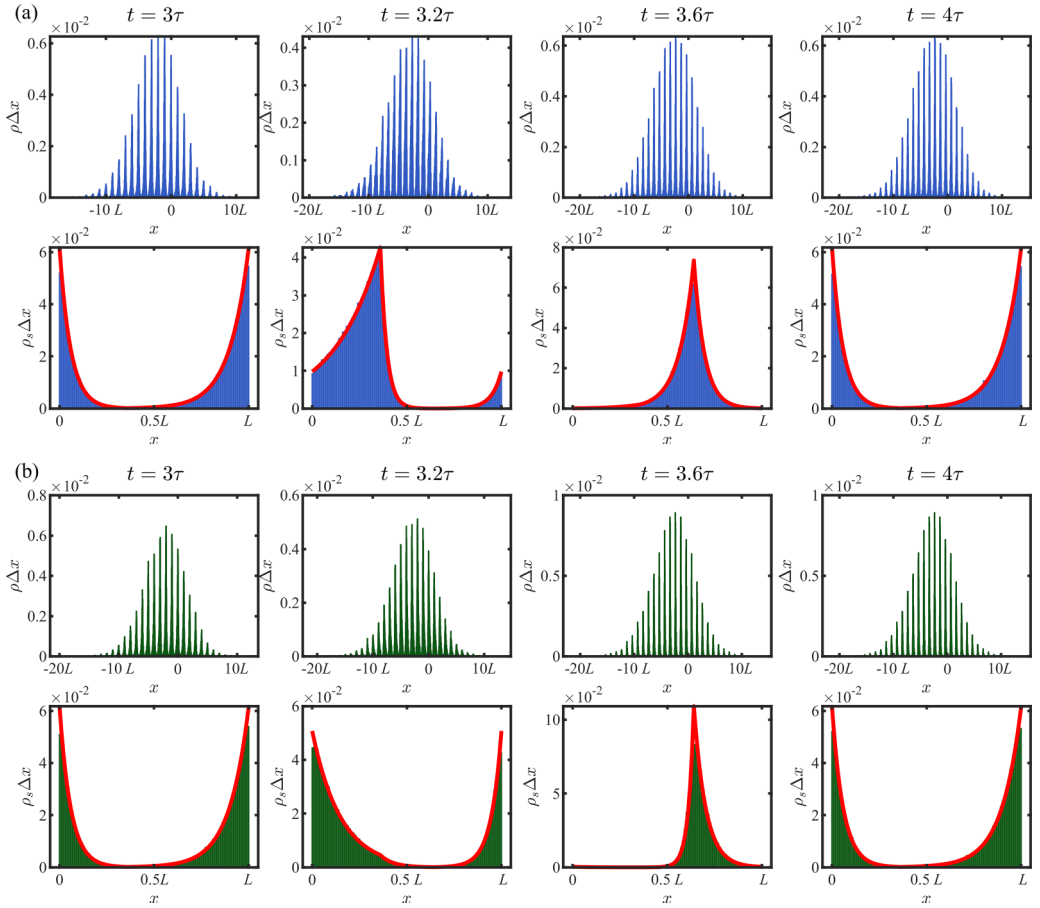

FIG. 10. Evolution of the steady-state distribution. The histograms in each subfigure's upper and lower panels represent actual and reduced distributions, respectively. The red solid lines are analytical predictions. (a) The distributions under the protocol along path II. (b) The distributions under the protocol along path III. The parameters in the simulations are $\tau = 20D^{*-1}L^2$, $D/D^* = 2$, $\beta = L = D^* = 1$, the particle number $N = 10^5$, and the time step $\Delta t = 10^{-4}D^{*-1}L^2$. The width of the histogram bars is $\Delta x = 10^{-2}L$. The initial distributions at $t = 0$ are uniform distributions on $x \in [0, L]$.

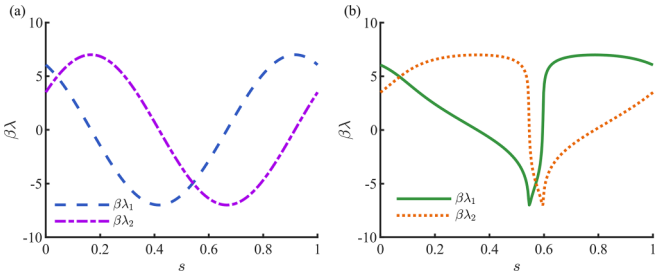

FIG. 11. Different driving protocols along the same loop. (a) A simple protocol expressed as trigonometric functions. (b) The optimal protocol.

4. Continuous limit of the heat current used in simulations

In the limit of $\Delta t \to 0$, the ensemble-averaged heat current given by Eq. (25) becomes

$$\begin{aligned}\dot{Q} &= \langle \dot{q} \rangle = \lim_{\Delta t \to 0} \left\langle \frac{\Delta q}{\Delta t} \right\rangle \\ &= \lim_{\Delta t \to 0} \left\langle \frac{U^*(x+\Delta x, t+\Delta t) - U^*(x, t+\Delta t)}{\Delta x} \frac{\Delta x}{\Delta t} \right\rangle \\ &= \left\langle \frac{\partial U^*(x,t)}{\partial x} \dot{x} \right\rangle \\ &= \int \rho(x,t) \frac{\partial U^*(x,t)}{\partial x} \frac{J(x,t)}{\rho(x,t)} dx \\ &= U^*(x,t) J(x,t)\big|_{-\infty}^{+\infty} - \int U^*(x,t) \frac{\partial J(x,t)}{\partial x} dx \\ &= \int U^*(x,t) \frac{\partial \rho(x,t)}{\partial t} dx, \end{aligned} \tag{D11}$$

where $\langle \cdots \rangle$ represents the average over different particle trajectories and we have used the natural boundary condition that the physical current $J(x,t)$ vanishes at infinity. This is exactly the same with the definition of continuous heat current (16) we used in the theoretical derivations.

5. Determine the optimal driving protocol

The optimal protocol $\vec{\lambda}(t)$ associated with the driving loop $\beta\lambda_1 = \beta R \cos(2\pi f(s) + \theta_0)$ and $\beta\lambda_2 = \beta R \sin(2\pi f(s) + \theta_0)$ can be numerically obtained from the equation

$$\Delta s = \frac{\sqrt{\Delta\lambda_\alpha \Delta\lambda_\beta G_{\alpha\beta}(\vec{\lambda})}}{\mathcal{L}} \equiv \Delta l, \tag{D12}$$

where $s \equiv t/\tau$. Since the thermodynamic length $\mathcal{L} = \int_0^\tau dt \sqrt{\dot{\lambda}_\alpha \dot{\lambda}_\beta G_{\alpha\beta}(\vec{\lambda})}$ is independent of the protocol [66,67], we first calculate the value of $\mathcal{L}$ and generate a series of $\vec{\lambda}$, namely, $\{\vec{\lambda}^{(i)}\}$, at $s = 0, \Delta, 2\Delta, \ldots, i\Delta, \ldots, n\Delta \equiv 1$ with a simple driving protocol $f(s) = s$ [shown in Fig. 11(a)]. Here Δ is a small positive interval, $n \in \mathbb{Z}$ and $0 \leqslant i \leqslant n$. Then we calculate the value of $\Delta l^{(j)}$ from $\vec{\lambda}^{(j-1)}$ to $\vec{\lambda}^{(j)}$, which gives the optimal variation of s denoted by $\Delta s_{\rm op}^{(j)}$ through Eq. (D12). Combining the series $\{\vec{\lambda}^{(i)}\}$ and $\{0, s_{\rm op}^{(i)} = \sum_{j=1}^{i} \Delta s_{\rm op}^{(j)}\}$, one obtains the optimal driving protocol illustrated in Fig. 11(b).

APPENDIX E: DETAILS FOR PRACTICAL CONSIDERATION

1. The flashing ratchet

The flashing ratchet is noncontinuous in time, as $U_s(x,t) = g(t)V(x)$, with

$$V(x) = \begin{cases} V_{\max} \frac{x}{x_c L}, & 0 \leqslant x < x_c L \\ V_{\max} \frac{L-x}{L-x_c L}, & x_c L \leqslant x < L, \end{cases}$$
$$g(t) = \begin{cases} 1, & 0 \leqslant t < r\tau \\ A, & r\tau \leqslant t < \tau. \end{cases} \tag{E1}$$

The parameters of $U_s(x,t)$ are set to be the same as those in Fig. 2 of Ref. [30]: $x_c = 0.7$, $\beta V_{\max} = 100$, $r = 0.25$, and $A = -0.5$.

2. The average extra power for three ratchets in simulations

The average power of extra work is defined as $P_{\rm ex} \equiv W_{\rm ex}/\tau$, where $W_{\rm ex} = W - \Delta E$ is the extra work in a period τ. For continuous ratchets $U^*(x,t)$ and $U_o(x,t)$, the energetic quantities in simulations are consistently obtained as Eqs. (25) and (26). The input work to the particles when using $U_s(x,t)$ is obtained by the variation of the internal energy when $g(t)$ undergoes a jump, that is,

$$W_{\rm jump} = \langle U_s(x, t_{\rm jump}^+) \rangle_{\rm jump} - \langle U_s(x, t_{\rm jump}^-) \rangle_{\rm jump}, \tag{E2}$$

where $t_{\rm jump} = r\tau, \tau$, and $\langle \cdots \rangle_{\rm jump}$ is the ensemble average under the distribution at $t = t_{\rm jump}$. There is no input work when $g(t)$ remains constant.

The data shown in Fig. 7(a) represent the total power required for simultaneously driving two different particles. To achieve minimal total extra work on a given driving loop, according to Eqs. (17)–(20), the optimal driving protocol for $U^*(x,t)$ ensures that $\sqrt{\dot{\lambda}_\alpha \dot{\lambda}_\beta [G^{(1)}_{\alpha\beta}(\vec{\lambda}) + G^{(2)}_{\alpha\beta}(\vec{\lambda})]}$ remains constant, where $G^{(1)}_{\alpha\beta}(\vec{\lambda})$ is the matrix for $D/D^* = 1/2$ and $G^{(2)}_{\alpha\beta}(\vec{\lambda})$ for $D/D^* = 2$. In addition, the data in Fig. 7(a) is obtained in the regime $\tilde{\tau} \in [1, 80]$ for $U^*(x,t)$, $\tilde{\tau} \in [0.22, 1.25]$ for $U_o(x,t)$, and $\tilde{\tau} \in [0.043, 0.0651]$ for $U_s(x,t)$.

[1] K. Khoshmanesh, S. Nahavandi, S. Baratchi, A. Mitchell, and K. Kalantar-zadeh, Dielectrophoretic platforms for bio-microfluidic systems, Biosens. Bioelectron. **26**, 1800 (2011).

[2] D. Zamboulis, E. N. Peleka, N. K. Lazaridis, and K. A. Matis, Metal ion separation and recovery from environmental sources using various flotation and sorption techniques, J. Chem. Technol. Biotechnol. **86**, 335 (2011).

[3] B. Kowalczyk, I. Lagzi, and B. A. Grzybowski, Nanoseparations: Strategies for size and/or shape-selective purification of nanoparticles, Curr. Opin. Colloid Interface Sci. **16**, 135 (2011).

[4] Y. Mori, Size-selective separation techniques for nanoparticles in liquid, KONA Powder Part. J. **32**, 102 (2015).

[5] D. S. Sholl and R. P. Lively, Seven chemical separations to change the world, Nature (London) **532**, 435 (2016).

[6] T. Makanyire, S. Sanchez-Segado, and A. Jha, Separation and recovery of critical metal ions using ionic liquids, Adv. Manuf. **4**, 33 (2016).

[7] S. Yang, F. Zhang, H. Ding, P. He, and H. Zhou, Lithium metal extraction from seawater, Joule **2**, 1648 (2018).

[8] H. Yoon, J. Lee, S. Kim, and J. Yoon, Review of concepts and applications of electrochemical ion separation (EIONS) process, Sep. Purif. Technol. **215**, 190 (2019).

[9] T. Mei, H. Zhang, and K. Xiao, Bioinspired artificial ion pumps, ACS Nano **16**, 13323 (2022).

[10] R. Ghosh, Protein separation using membrane chromatography: Opportunities and challenges, J. Chromatogr., A **952**, 13 (2002).

[11] Z. Zhu, J. J. Lu, and S. Liu, Protein separation by capillary gel electrophoresis: A review, Anal. Chim. Acta **709**, 21 (2012).

[12] R. Nouri and W. Guan, Nanofluidic charged-coupled devices for controlled DNA transport and separation, Nanotechnology **32**, 345501 (2021).

[13] S.-W. Choe, B. Kim, and M. Kim, Progress of microfluidic continuous separation techniques for micro-/nanoscale bioparticles, Biosensors **11**, 464 (2021).

[14] F. von der Kammer, S. Legros, T. Hofmann, E. H. Larsen, and K. Loeschner, Separation and characterization of nanoparticles in complex food and environmental samples by field-flow fractionation, TrAC Trends in Anal. Chem.Charact., Anal. Risks Nanomater. Environ. Food Samples II, **30**, 425 (2011).

[15] X. Zhang, K. Zuo, X. Zhang, C. Zhang, and P. Liang, Selective ion separation by capacitive deionization (CDI) based technologies: A state-of-the-art review, Environ. Sci.: Water Res. Technol. **6**, 243 (2020).

[16] S. S. Leong, Z. Ahmad, S. C. Low, J. Camacho, J. Faraudo, and J. Lim, Unified view of magnetic nanoparticle separation under magnetophoresis, Langmuir **36**, 8033 (2020).

[17] S. Hettiarachchi, H. Cha, L. Ouyang, A. Mudugamuwa, H. An, G. Kijanka, N. Kashaninejad, N.-T. Nguyen, and J. Zhang, Recent microfluidic advances in submicron to nanoparticle manipulation and separation, Lab Chip **23**, 982 (2023).

[18] K. Lee, R. Mishra, and T. Kim, Review of micro/nanofluidic particle separation mechanisms: Toward combined multiple physical fields for nanoparticles, Sens. Actuators A: Phys. **363**, 114688 (2023).

[19] S. Marbach and L. Bocquet, Active sieving across driven nanopores for tunable selectivity, J. Chem. Phys. **147**, 154701 (2017).

[20] H. B. Park, J. Kamcev, L. M. Robeson, M. Elimelech, and B. D. Freeman, Maximizing the right stuff: The trade-off between membrane permeability and selectivity, Science **356**, eaab0530 (2017).

[21] P. S. Goh, W. J. Lau, M. H. D. Othman, and A. F. Ismail, Membrane fouling in desalination and its mitigation strategies, Desalination **425**, 130 (2018).

[22] C. Tang and M. L. Bruening, Ion separations with membranes, J. Polym. Sci. **58**, 2831 (2020).

[23] R. Epsztein, R. M. DuChanois, C. L. Ritt, A. Noy, and M. Elimelech, Towards single-species selectivity of membranes with subnanometre pores, Nat. Nanotechnol. **15**, 426 (2020).

[24] D. Reguera, A. Luque, P. S. Burada, G. Schmid, J. M. Rubí, and P. Hänggi, Entropic splitter for particle separation, Phys. Rev. Lett. **108**, 020604 (2012).

[25] S. M. McFaul, B. K. Lin, and H. Ma, Cell separation based on size and deformability using microfluidic funnel ratchets, Lab Chip **12**, 2369 (2012).

[26] L. Bogunovic, R. Eichhorn, J. Regtmeier, D. Anselmetti, and P. Reimann, Particle sorting by a structured microfluidic ratchet device with tunable selectivity: Theory and experiment, Soft Matter **8**, 3900 (2012).

[27] C. Murray, E. Pao, P. Tseng, S. Aftab, R. Kulkarni, M. Rettig, and D. Di Carlo, Quantitative magnetic separation of particles and cells using gradient magnetic ratcheting, Small **12**, 1891 (2016).

[28] A. Słapik, J. Łuczka, P. Hänggi, and J. Spiechowicz, Tunable mass separation via negative mobility, Phys. Rev. Lett. **122**, 070602 (2019).

[29] P. Nicollier, C. Schwemmer, F. Ruggeri, D. Widmer, X. Ma, and A. W. Knoll, Nanometer-scale-resolution multichannel separation of spherical particles in a rocking ratchet with increasing barrier heights, Phys. Rev. Appl. **15**, 034006 (2021).

[30] A. Herman, J. W. Ager, S. Ardo, and G. Segev, Ratchet-based ion pumps for selective ion separations, PRX Energy **2**, 023001 (2023).

[31] M. Smoluchowski, Experimentell nachweisbare, der üblichen Thermodynamik widersprechende Molekularphänomene, Physik. Zeitschr. **13**, 1069 (1912).

[32] R. P. Feynman, R. Leighton, and M. Sands, *The Feynman Lectures on Physics, Vol. I: The New Millennium Edition: Mainly Mechanics, Radiation, and Heat* (Basic Books, New York, 2011).

[33] P. Reimann, Brownian motors: Noisy transport far from equilibrium, Phys. Rep. **361**, 57 (2002).

[34] M. O. Magnasco, Forced thermal ratchets, Phys. Rev. Lett. **71**, 1477 (1993).

[35] J. Rousselet, L. Salome, A. Ajdari, and J. Prostt, Directional motion of Brownian particles induced by a periodic asymmetric potential, Nature (London) **370**, 446 (1994).

[36] R. D. Astumian and M. Bier, Fluctuation driven ratchets: Molecular motors, Phys. Rev. Lett. **72**, 1766 (1994).

[37] R. Bartussek, P. Hänggi, and J. G. Kissner, Periodically rocked thermal ratchets, Europhys. Lett. **28**, 459 (1994).

[38] C. R. Doering, Randomly rattled ratchets, Il Nuovo Cimento D **17**, 685 (1995).

[39] F. Jülicher, A. Ajdari, and J. Prost, Modeling molecular motors, Rev. Mod. Phys. **69**, 1269 (1997).

[40] J. M. R. Parrondo, Reversible ratchets as Brownian particles in an adiabatically changing periodic potential, Phys. Rev. E **57**, 7297 (1998).

[41] I. M. Sokolov, Irreversible and reversible modes of operation of deterministic ratchets, Phys. Rev. E **63**, 021107 (2001).

[42] V. M. Rozenbaum, High-temperature Brownian motors: Deterministic and stochastic fluctuations of a periodic potential, JETP Lett. **88**, 342 (2008).

[43] Y. V. Gulyaev, A. S. Bugaev, V. M. Rozenbaum, and L. I. Trakhtenberg, Nanotransport controlled by means of the ratchet effect, Phys. Usp. **63**, 311 (2020).

[44] L. P. Faucheux and A. Libchaber, Selection of Brownian particles, J. Chem. Soc., Faraday Trans. **91**, 3163 (1995).

[45] J. S. Bader, R. W. Hammond, S. A. Henck, M. W. Deem, G. A. McDermott, J. M. Bustillo, J. W. Simpson, G. T. Mulhern, and J. M. Rothberg, DNA transport by a micromachined Brownian ratchet device, Proc. Natl. Acad. Sci. **96**, 13165 (1999).

[46] C. Kettner, P. Reimann, P. Hänggi, and F. Müller, Drift ratchet, Phys. Rev. E **61**, 312 (2000).

[47] S. Matthias and F. Müller, Asymmetric pores in a silicon membrane acting as massively parallel Brownian ratchets, Nature (London) **424**, 53 (2003).

[48] S. Savel'ev, V. Misko, F. Marchesoni, and F. Nori, Separating particles according to their physical properties: Transverse drift of underdamped and overdamped interacting particles diffusing through two-dimensional ratchets, Phys. Rev. B **71**, 214303 (2005).

[49] B. J. Lopez, N. J. Kuwada, E. M. Craig, B. R. Long, and H. Linke, Realization of a feedback controlled flashing ratchet, Phys. Rev. Lett. **101**, 220601 (2008).

[50] O. Kedem, B. Lau, and E. A. Weiss, How to drive a flashing electron ratchet to maximize current, Nano Lett. **17**, 5848 (2017).

[51] B. Lau and O. Kedem, Electron ratchets: State of the field and future challenges, J. Chem. Phys. **152**, 200901 (2020).

[52] V. M. Rozenbaum, T. Y. Korochkova, A. A. Chernova, and M. L. Dekhtyar, Brownian motor with competing spatial and temporal asymmetry of potential energy, Phys. Rev. E **83**, 051120 (2011).

[53] A. M. Tsirlin, V. Kazakov, and D. V. Zubov, Finite-time thermodynamics: Limiting possibilities of irreversible separation processes, J. Phys. Chem. A **106**, 10926 (2002).

[54] Y. Huang, R. W. Baker, and L. M. Vane, Low-energy distillation-membrane separation process, Ind. Eng. Chem. Res. **49**, 3760 (2010).

[55] J.-F. Chen, R.-X. Zhai, C. P. Sun, and H. Dong, Geodesic lower bound of the energy consumption to achieve membrane separation within finite time, PRX Energy **2**, 033003 (2023).

[56] D. Guéry-Odelin, A. Ruschhaupt, A. Kiely, E. Torrontegui, S. Martínez-Garaot, and J. G. Muga, Shortcuts to adiabaticity: Concepts, methods, and applications, Rev. Mod. Phys. **91**, 045001 (2019).

[57] D. Guéry-Odelin, C. Jarzynski, C. A. Plata, A. Prados, and E. Trizac, Driving rapidly while remaining in control: Classical shortcuts from Hamiltonian to stochastic dynamics, Rep. Prog. Phys. **86**, 035902 (2023).

[58] M. Demirplak and S. A. Rice, Adiabatic population transfer with control fields, J. Phys. Chem. A **107**, 9937 (2003).

[59] M. V. Berry, Transitionless quantum driving, J. Phys. A: Math. Theor. **42**, 365303 (2009).

[60] A. del Campo, Shortcuts to adiabaticity by counterdiabatic driving, Phys. Rev. Lett. **111**, 100502 (2013).

[61] C. Jarzynski, Generating shortcuts to adiabaticity in quantum and classical dynamics, Phys. Rev. A **88**, 040101(R) (2013).

[62] S. Deffner, C. Jarzynski, and A. del Campo, Classical and quantum shortcuts to adiabaticity for scale-invariant driving, Phys. Rev. X **4**, 021013 (2014).

[63] G. Li, H. T. Quan, and Z. C. Tu, Shortcuts to isothermality and nonequilibrium work relations, Phys. Rev. E **96**, 012144 (2017).

[64] G. Li, J.-F. Chen, C. P. Sun, and H. Dong, Geodesic path for the minimal energy cost in shortcuts to isothermality, Phys. Rev. Lett. **128**, 230603 (2022).

[65] G. Li and Z. C. Tu, Nonequilibrium work relations meet engineered thermodynamic control: A perspective for nonequilibrium measurements, Europhys. Lett. **142**, 61001 (2023).

[66] P. Salamon and R. S. Berry, Thermodynamic length and dissipated availability, Phys. Rev. Lett. **51**, 1127 (1983).

[67] G. E. Crooks, Measuring thermodynamic length, Phys. Rev. Lett. **99**, 100602 (2007).

[68] D. A. Sivak and G. E. Crooks, Thermodynamic metrics and optimal paths, Phys. Rev. Lett. **108**, 190602 (2012).

[69] L. E. Reichl, *A Modern Course in Statistical Physics*, 4th edition (Wiley-VCH, Weinheim, 2016).

[70] V. Cavina, A. Mari, and V. Giovannetti, Slow dynamics and thermodynamics of open quantum systems, Phys. Rev. Lett. **119**, 050601 (2017).

[71] Y.-H. Ma, J.-F. Chen, C. P. Sun, and H. Dong, Minimal energy cost to initialize a bit with tolerable error, Phys. Rev. E **106**, 034112 (2022).

[72] J. Parrondo and B. de Cisneros, Energetics of Brownian motors: A review, Appl. Phys. A **75**, 179 (2002).

[73] V. M. Rozenbaum, I. V. Shapochkina, and L. I. Trakhtenberg, Green's function method in the theory of Brownian motors, Phys. Usp. **62**, 496 (2019).

[74] T. C. Chan, H. T. Li, and K. Y. Li, Effects of shapes of solute molecules on diffusion: A study of dependences on solute size, solvent, and temperature, J. Phys. Chem. B **119**, 15718 (2015).

[75] S. Miyamoto and K. Shimono, Molecular modeling to estimate the diffusion coefficients of drugs and other small molecules, Molecules **25**, 5340 (2020).

[76] K. Sekimoto, *Stochastic Energetics*, Lecture Notes in Physics, Vol. 799 (Springer, Berlin, Heidelberg, 2010).

[77] U. Seifert, Stochastic thermodynamics, fluctuation theorems and molecular machines, Rep. Prog. Phys. **75**, 126001 (2012).

[78] Y.-H. Ma, R.-X. Zhai, J. Chen, C. P. Sun, and H. Dong, Experimental test of the $1/\tau$-scaling entropy generation in finite-time thermodynamics, Phys. Rev. Lett. **125**, 210601 (2020).

[79] R. Zwanzig, *Nonequilibrium Statistical Mechanics* (Oxford University Press, New York, 2001).

[80] A. C. Brańka and D. M. Heyes, Algorithms for Brownian dynamics simulation, Phys. Rev. E **58**, 2611 (1998).

[81] M. Esposito, R. Kawai, K. Lindenberg, and C. Van den Broeck, Efficiency at maximum power of low-dissipation Carnot engines, Phys. Rev. Lett. **105**, 150603 (2010).

[82] I. A. Martínez, É. Roldán, L. Dinis, D. Petrov, J. M. Parrondo, and R. A. Rica, Brownian Carnot engine, Nat. Phys. **12**, 67 (2016).

[83] H. Yuan, Y.-H. Ma, and C. P. Sun, Optimizing thermodynamic cycles with two finite-sized reservoirs, Phys. Rev. E **105**, L022101 (2022).

[84] V. M. Rozenbaum, Y. A. Makhnovskii, I. V. Shapochkina, S.-Y. Sheu, D.-Y. Yang, and S. H. Lin, Adiabatically slow and adiabatically fast driven ratchets, Phys. Rev. E **85**, 041116 (2012).

[85] M. Wiśniewski and J. Spiechowicz, Memory-induced absolute negative mobility, arXiv:2405.17911.

[86] V. Rouco, A. Palau, C. Monton, N. Del-Valle, C. Navau, A. Sanchez, X. Obradors, and T. Puig, Geometrically controlled ratchet effect with collective vortex motion, New J. Phys. **17**, 073022 (2015).

[87] Marcos, H. C. Fu, T. R. Powers, and R. Stocker, Separation of microscale chiral objects by shear flow, Phys. Rev. Lett. **102**, 158103 (2009).

[88] C. Bechinger, R. Di Leonardo, H. Löwen, C. Reichhardt, G. Volpe, and G. Volpe, Active particles in complex and crowded environments, Rev. Mod. Phys. **88**, 045006 (2016).

[89] N. Khatri and R. Kapral, Inertial effects on rectification and diffusion of active Brownian particles in an asymmetric channel, J. Chem. Phys. **158**, 124903 (2023).

[90] D. M. Busiello, S. Liang, F. Piazza, and P. De Los Rios, Dissipation-driven selection of states in non-equilibrium chemical networks, Commun. Chem. **4**, 16 (2021).

[91] J. A. C. Albay, S. R. Wulaningrum, C. Kwon, P.-Y. Lai, and Y. Jun, Thermodynamic cost of a shortcuts-to-isothermal transport of a Brownian particle, Phys. Rev. Res. **1**, 033122 (2019).

[92] J. A. C. Albay, P.-Y. Lai, and Y. Jun, Realization of finite-rate isothermal compression and expansion using optical feedback trap, Appl. Phys. Lett. **116**, 103706 (2020).

[93] S. Savel'ev, F. Marchesoni, P. Hänggi, and F. Nori, Transport via nonlinear signal mixing in ratchet devices, Phys. Rev. E **70**, 066109 (2004).

[94] V. M. Rozenbaum, I. V. Shapochkina, Y. Teranishi, and L. I. Trakhtenberg, High-temperature ratchets driven by deterministic and stochastic fluctuations, Phys. Rev. E **99**, 012103 (2019).

[95] G. Patil, P. Mandal, and A. Ghosh, Using the thermal ratchet mechanism to achieve net motility in magnetic microswimmers, Phys. Rev. Lett. **129**, 198002 (2022).

[96] A. V. Arzola, K. Volke-Sepúlveda, and J. L. Mateos, Experimental control of transport and current reversals in a deterministic optical rocking ratchet, Phys. Rev. Lett. **106**, 168104 (2011).

[97] S.-H. Wu, N. Huang, E. Jaquay, and M. L. Povinelli, Near-field, on-chip optical Brownian ratchets, Nano Lett. **16**, 5261 (2016).

[98] Y.-H. Ma, D. Xu, H. Dong, and C.-P. Sun, Optimal operating protocol to achieve efficiency at maximum power of heat engines, Phys. Rev. E **98**, 022133 (2018).

[99] A. G. Frim and M. R. DeWeese, Geometric bound on the efficiency of irreversible thermodynamic cycles, Phys. Rev. Lett. **128**, 230601 (2022).

[100] X.-H. Zhao, Z.-N. Gong, and Z. C. Tu, Low-dissipation engines: Microscopic construction via shortcuts to adiabaticity and isothermality, the optimal relation between power and efficiency, Phys. Rev. E **106**, 064117 (2022).

[101] A. Rolandi, P. Abiuso, and M. Perarnau-Llobet, Collective advantages in finite-time thermodynamics, Phys. Rev. Lett. **131**, 210401 (2023).

[102] I. A. Martínez, A. Petrosyan, D. Guéry-Odelin, E. Trizac, and S. Ciliberto, Engineered swift equilibration of a Brownian particle, Nat. Phys. **12**, 843 (2016).

[103] K. Nakamura, J. Matrasulov, and Y. Izumida, Fast-forward approach to stochastic heat engine, Phys. Rev. E **102**, 012129 (2020).